Geophys. J. R. astr. Soc. (1983) **75**, 799–837

A lower mantle *S*-wave triplication and the shear velocity structure of D″

Thorne Lay and Donald V. Helmberger *Seismological Laboratory, California Institute of Technology, Pasadena, California 91125, USA*

Received 1983 April 15; in original form 1982 September 14

Summary. A lower mantle *S*-wave triplication detected with short- and long-period WWSSN and CSN recordings indicates a substantial shear velocity discontinuity near 280 km above the core–mantle boundary. The triplication can be observed in rotated *SH* seismograms from intermediate and deep focus events throughout the distance range from 70° to 95°. Three distinct source region–receiver array combinations that have been investigated in detail demonstrate consistent travel time and relative amplitude behaviour of the triplication, with slight systematic shifts in the triplication indicating up to 40 km variations in the depth of the discontinuity. Modelling of the observations with synthetic seismograms produced with the Cagniard de Hoop and reflectivity methods constrains the shear velocity increase to be 2.75 ± 0.25 per cent, comparable to upper mantle discontinuities. Short-period observations indicate that the velocity increase may be a sharp first-order discontinuity, or may extend over a transition zone no more than 50 km thick. The shear velocity gradient below the discontinuity, within the D″ layer, is not well-constrained by the *SH* data, but slightly positive or near zero velocity gradients are consistent with the long-period amplitude ratios of *ScSH/SH*.

Introduction

The lowermost 200 km of the mantle (D″ region) has long been associated with anomalously low shear velocity gradients and increased scatter in travel times and amplitudes of *S*-waves (Bullen 1949; Cleary, Porra & Read 1967; Hales & Roberts 1970). Gross earth models determined from travel times and free oscillations (e.g. Bullen 1963; Sengupta 1975; Gilbert & Dziewonski 1975; Anderson & Hart 1976; Dziewonski & Anderson 1981) have generally indicated very smooth lower mantle velocity structures with mild positive or near zero shear velocity gradients within D″. Early investigations of diffracted *SH*-wave travel times, relying on classical ray theory interpretations, suggested very low *S*-wave velocities at the core–mantle boundary (CMB) and attendant strong negative velocity gradients above the boundary (Cleary *et al.* 1967; Cleary 1969; Bolt, Niazi & Somerville 1970; Hales & Roberts 1970). However, recent studies of diffracted *S* utilizing more complete diffraction theory

and synthetic modelling capabilities have found milder positive or negative shear velocity gradients in D″, generally compatible with the gross earth models (Mondt 1977; Doornbos & Mondt 1979; Okal & Geller 1979; Mula & Müller 1980). There is little agreement in the fine details of the various shear velocity models that have been determined for the base of the mantle, which may reflect the actual heterogeneity of the region, or possibly the limited resolution of the free oscillation, travel time and diffracted wave analyses which have been performed. No study of the shear velocity structure in the lower mantle has indicated any significant discontinuity near the top of D″, other than smooth changes in the velocity gradient. There is clearly a large amount of lateral averaging in all of these studies, and regional variations in D″ would be difficult to resolve. Any fine velocity structure such as small discontinuities, even of a global nature, could also have been completely missed because of the rather subtle effects produced by lower mantle structure.

Determination of the lower mantle shear velocity structure is complicated by the high attenuation of *S* phases in the mantle, the arrival of late *P* phases, and the contamination of direct *S* arrivals by *SKS*, which crosses over and arrives ahead of *SV* beyond 82°. Yet, *S*-waves have a major advantage over *P*-waves for D″ studies, in that the intrinsically lower shear velocities help to separate the arrivals produced by any fine structure, allowing discrete phases to be observed. Utilizing *SH* phases reduces the contamination of late *P* and *SKS* arrivals. In addition, the *ScSH* phase is completely reflected at the core and is easily observable, unlike *PcP* which is hard to identify over large distance ranges. Several recent attempts to utilize *P*-waves to resolve fine structure of the lower mantle indicate that there is significant *P*-wave velocity structure within D″ (Ruff & Helmberger 1982; Wright & Lyons 1979, 1981); however, substantial data processing is necessary to isolate the subtle effects of this fine structure on the *P*-waves. In this paper we present a large body of *S*-wave data which show clear evidence for major shear wave velocity structure at the top of D″. In addition, since we utilize direct body wave phases which sample relatively localized regions of the lower mantle, we are able to quantify lateral variations in D″ for three distinct regions. These results yield the important conclusion that the D″ region is stratified, possibly on a global scale, with either a phase change or compositional change from the mantle above it. Thus, a simple model of the D″ region as a thermal boundary layer with diminished velocity gradients caused by a superadiabatic thermal gradient is unwarranted.

The shear velocity models that have been proposed for the lower mantle are generally very smooth below 1000 km depth, with the only major features being low velocity zones at the base of the mantle in the few models which incorporated early estimates of the diffracted *S*-ray parameter (Randall 1971; Robinson & Kovach 1972). All other features in the velocity models are too small to produce a triplication or observable *S*-wave reflections. Thus, for an intermediate or deep focus earthquake, no *SH* arrival is predicted between direct *S* and *ScS* at distances large enough that all surface reflections arrive after *ScS*. This is generally substantiated by data as can be seen in Fig. 1. The data are rotated tangential component seismograms recorded at long period WWSSN and Canadian Seismic Network (CSN) stations in North America. The Sea of Okhostsk event shown has a focal depth of 583 km, and *sS* arrives later than *ScS* at distances greater than 44°. The *SH* radiation to North America is near the maximum for both *S* and *ScS* so each phase is clearly observable. Note the lack of any coherent arrival between *S* and *ScS* in the range 44–70° that could be attributed to either source or deep mantle structure. There is appreciable receiver structure at some stations, notably BKS and COR, but, in general, the signals are quite simple and coherent. This coherence reflects the fact that the stations lie in a narrow azimuth range in a stable portion of the radiation pattern for this event. However, beyond 70° there is a systematic arrival between *S* and *ScS*, indicated by the arrows, which interferes with the down-

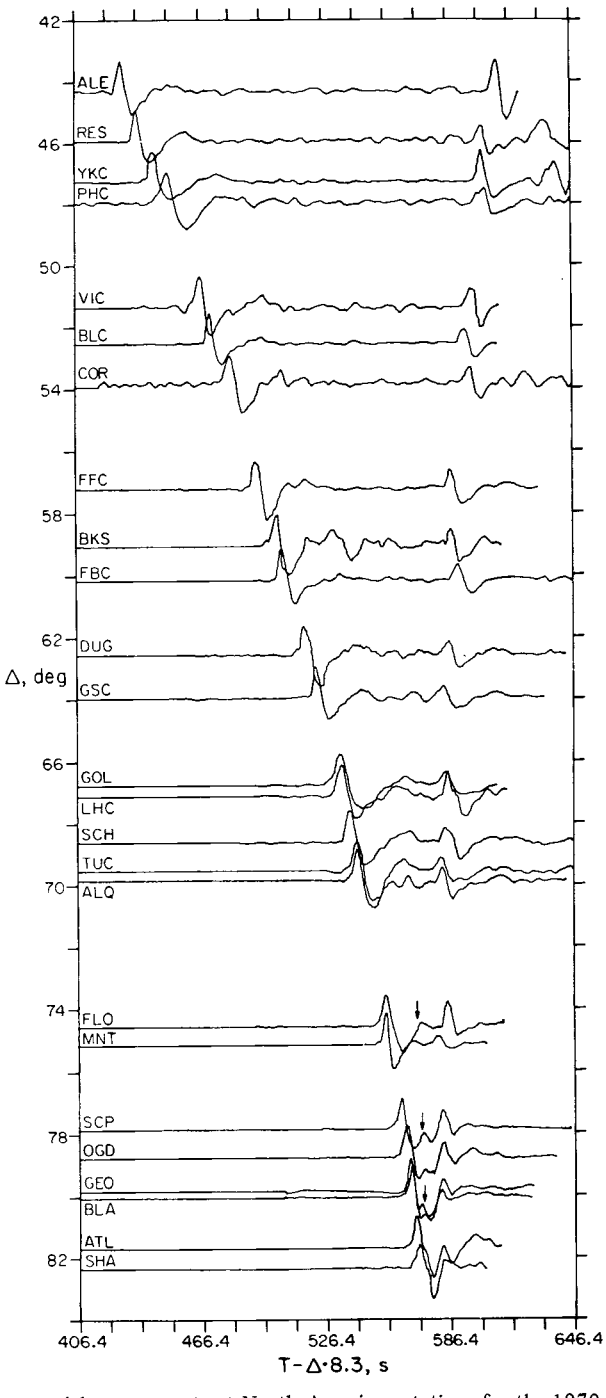

Figure 1. Profile of tangential components at North American stations for the 1970 September 5, Sea of Okhotsk event ($d = 583$ km). Direct S is the first large arrival in each trace with ScS arriving around 580–600 s. Station JB travel-time anomalies have been removed and the amplitudes are normalized. The arrows indicate the arrival of an ScS precursor shown in greater detail in Fig. 6.

swing of direct *S*, and appears to maintain a nearly constant separation from *ScS*. This feature is investigated in detail below, to determine whether it is due to source complexity, receiver structure, or lower mantle structure. Before proceeding with the data analysis, it is instructive to determine what features a lower mantle discontinuiuty would produce in a profile of *SH* data like that in Fig. 1.

Since the Jeffreys-Bullen (1940) *S*-wave travel times have proved a reliable standard for lower mantle paths (e.g. Doyle & Hales 1967; Hales & Roberts 1970; Dziewonski & Anderson 1981) we adopt the JB model of Press (1966) as a reference model. This model has smooth shear velocity gradients throughout the mantle except for a zero gradient within D″. The only systematic departure of more recent data sets from the JB *S*-wave model in the range 40–100° is that beyond 80° the JB times are progressively early by several seconds (see Sengupta 1975, figs 3–17 and 3–19 for a comparison of various models). For a surface focus event, an *S*-wave travelling 80° bottoms at a depth around 2200 km in the mantle. Therefore, below this depth it appears that the JB model is too fast. The core radius in the JB model (3473 km) also is slightly inconsistent with more recent estimates from *PcP* and free oscillations (Dziewonski & Haddon 1974) and is increased to 3485 km in the models determined in this paper.

Fig. 2 shows the lower 700 km of the mantle shear wave structure for the JB model and for a model with a 2.75 per cent velocity discontinuity 278 km above the CMB. The latter model, SLHO, is actually that derived for the *SH* data from Sea of Okhotsk events recorded in North America, as shown below. The presence of the large, sharp discontinuity produces a triplication not produced by the JB model. Synthetic *SH* seismograms for these two velocity structures are compared in Fig. 3. The synthetics are computed using the Cagniard de

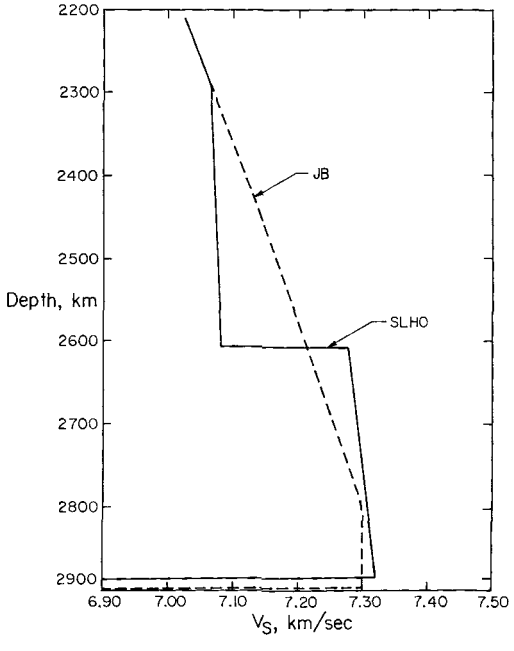

Figure 2. Velocity profiles of the reference JB model and model SLHO which is derived from the Sea of Okhotsk data recorded in North America. The core radius for SLHO is 12 km greater than for the JB model. The velocity discontinuity 278 km above the core in model SLHO is a 2.75 per cent increase. The models are identical above 2200 km.

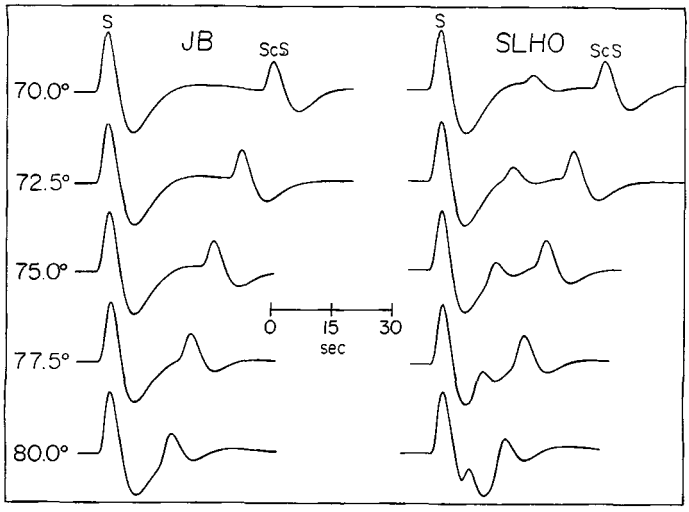

Figure 3. Synthetic long period tangential component *S*-waves for a 580 km deep source. The traces are aligned on the direct *S* arrival and the amplitudes are normalized. The synthetics on the left were generated using the JB model, which has smooth velocity gradients in the lower mantle and only produces the *S* and *ScS* phases. Those on the right were generated for model SLHO in Fig. 2, which produces the additional triplication arrival between *S* and ScS. Note that this phase must be very strong at 80° to produce the clear distortion of the *S*-wave downswing.

Hoop generalized ray theory method as discussed by Helmberger (1974). For the smooth JB model the only two arrivals predicted are direct *S* and *ScS*. The triplication produced by model SLHO produces the arrival between *ScS* and *S*. This arrival, which corresponds to the *Scd* branch in standard triplication terminology (see Fig. 14), is small near 70° and is virtually unobservable at closer distances, particularly given the typical noise level between *S* and *ScS* shown in Fig. 1. By 75°, *Scd* is quite large, and it begins to interfere with the direct *S* (*Sab*) arrival. At 80° *Scd* is apparent in the downswing of the direct arrival and a strong interference is apparent. Note that the second arrival is actually very large, for it sharply turns the instrument downswing of the *Sab* arrival. At this range the *Scd* arrival is as large as *ScS*, though because of the interference with *Sab*, the arrival is somewhat obscured. This type of interference pattern is what should be looked for in the *SH* data in this distance range.

Sea of Okhotsk data recorded in North America

The most complete *S*-wave data set that we have gathered is for 10 intermediate and deep focus events in the Sea of Okhotsk recorded at WWSSN and CSN stations in North America. The epicentres and stations are shown in Fig. 4, and the hypocentral coordinates are listed in Table 1. All events since 1963 with $m_b \geq 5.5$ and focal depths greater than 100 km along the Kurile trench were examined in collecting these data. The selection criteria imposed were: stable *SH* radiation patterns to North America, simple impulsive waveforms indicative of minimal source complexity, and adequate station coverage to provide dense profiles in the range of 45–90°. All short- and long-period horizontal components which could be recovered were digitized over the time interval from direct *S* to *ScS* and rotated into tangential and radial components. This yielded data profiles similar to those in Fig. 1, for both short and long periods. While we have found that the direct evidence for a lower mantle triplication is apparent in the data only at distances greater than 68°, as suggested in

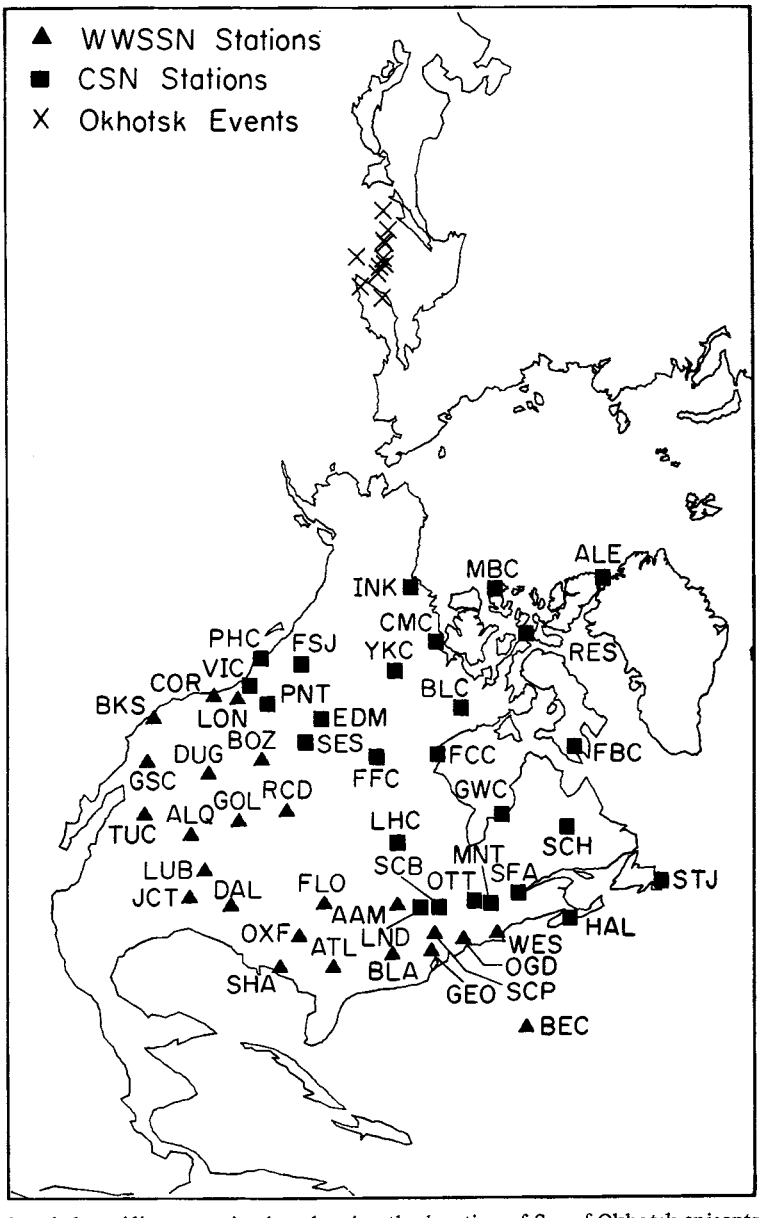

Figure 4. Azimuthal equidistant projection showing the location of Sea of Okhotsk epicentres and North American stations used in this study. Station SHA ranges from 78° to 88° from the events.

Fig. 3, inspection of the *S* and *ScS* signals at closer distances has provided a means by which to better assess the source complexity of each event.

As shown in Fig. 4, the North American stations span about 50° in azimuth from the Okhotsk source region, along the strike of the subducting slab. Since most of the source mechanisms have a *P*-wave nodal plane with a strike similar to that of the slab, the *SH* radiation is very stable to North America for both *S* and *ScS*. This is indicated in Fig. 5, which shows the nodal radiation orientations for *P*, *SV* and *SH* signals for several of the

Table 1. Source parameters for events used in this study.

Region	Date	Origin Time	Latitude	Longitude	Depth, km	Reference	Number
Sea of Okhotsk	18 Mar. 1964	04:37:25.7 ± 0.08	52.56° ± 0.022°N	153.67° ± 0.030°E	424 ± 4.2	ISC	1
	12 Oct. 1967	12:53:45.9 ± 0.21	52.15° ± 0.018°N	152.57° ± 0.025°E	466 ± 2.7	ISC	2
	1 Dec. 1967	13:57:02.4	49.5°N	154.4°E	136	NOAA	3
	5 Sep. 1970	07:52:32.4	52.32°N	151.46°E	583	Strelitz (1975)	4
	29 Jan. 1971	21:58:06.7	51.72° ± 0.032°N	151.04° ± 0.024°E	540 ± 5.7	Veith (1974)	5
	27 May 1972	04:06:49.6 ± 0.25	54.97° ± 0.013°N	156.33° ± 0.020°E	397 ± 2.8	ISC	6
	21 Aug. 1972	06:23:48.6 ± 0.16	49.47° ± 0.012°N	147.08° ± 0.019°E	573 ± 2.2	ISC	7
	28 Jul. 1973	20:06:35.4 ± 0.15	50.45° ± 0.013°N	148.92° ± 0.022°E	585 ± 2.1	ISC	8
	21 Sep. 1974	15:54:59.1 ± 0.37	52.19° ± 0.016°N	157.44° ± 0.023°E	119 ± 3.5	ISC	9
	10 Jul. 1976	11:37:14.0 ± 0.14	47.31° ± 0.011°N	145.75° ± 0.018°E	402 ± 1.7	ISC	10
Sea of Japan	31 Mar. 1969	19:25:27.2	33.31°N	134.50°W	417	NOAA	11
	10 Sep. 1973	07:43:30.5	42.45°N	130.91°W	532	NOAA	12
Argentina	9 Dec. 1964	13:35:42.4	27.5°S	63.2°W	586	NOAA	13
	5 Mar. 1965	14:32:19.2	27.0°S	63.3°W	573	NOAA	14
	20 Dec. 1966	12:26:54.6	26.1°S	63.2°W	586	NOAA	15
	17 Jan. 1967	01:07:54.3	27.4°S	63.3°W	588	NOAA	16
	9 Sep. 1967	10:06:44.1	27.7°S	63.1°W	578	NOAA	17
	25 Jul. 1969	06:06:42.4	25.6°S	63.3°W	579	NOAA	18
	3 Jan. 1973	02:58:16.7	27.7°S	63.3°W	563	NOAA	19

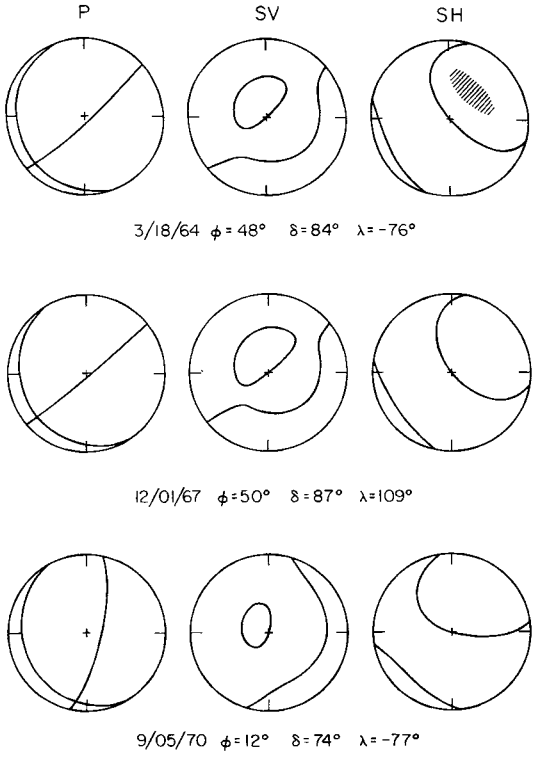

Figure 5. Radiation patterns for three of the Sea of Okhotsk events. The nodal lines are plotted in the lower hemisphere of equal area projections. The hatchured area indicates the portion of the focal sphere covered by North American *S* and *ScS* observations. For the top two events both *P* and *SV* are nodal in this region, whereas for the bottom event *SV* and *SH* are comparably stable.

events used. The hatchured region in the *SH* mechanism for the first event indicates the portion of the focal sphere covered by *S* and *ScS* rays to North American stations.

P-wave first motion mechanisms for each event were taken from the literature or newly determined and the observed long-period *SV*/*SH* amplitude ratios were used to redetermine each mechanism. This allowed us to refine the mechanisms and to select between conflicting

Table 2. Fault plane orientations.

Date	Strike (°)	Dip (°)	Rake (°)
9 Dec. 1964	171	78	-90
5 Mar. 1965	12	26	-68
20 Dec. 1966	30	43	-42
17 Jan. 1967	28	30	-44
9 Sep. 1967	3	19	-78
3 Jan. 1973	357	28	-83
18 Mar. 1964	48	84	-76
12 Oct. 1967	30	75	-52
1 Dec. 1967	50	87	109
5 Sep. 1970	12	74	-77
29 Jan. 1971	40	77	-119
27 May 1972	25	82	-93
21 Aug. 1972	18	19	44
28 Jul. 1973	51	76	-107
21 Sep. 1974	205	79	80
10 Jul. 1976	40	81	-87

mechanisms given in the literature for each event. The final mechanisms adopted are listed in Table 2. Six of the events have mechanisms very similar to that of 1964 March 18, shown in Fig. 5. Both *P* and *SV* are nodal in North America for these events. Two of the intermediate depth events have mechanisms similar to that of 1967 December 1, which has the same orientation as the others, but an opposite sense of motion. For two events, those of 1970 September 5, and 1971 January 1, the mechanisms are slightly rotated, which yields stable *SH* as well as stable *SV* radiation to North America. This is a fortunate occurrence, enabling us to inspect the *SV* data as well. The nodal character of the *P* and *SV* radiation for most of the events helps to minimize the complications due to late *P* arrivals and *SKS*. The long-period *SH* signals generally rotate very well and appear to be free of anomalous effects due to mismatched horizontal components. The short-period signals tend to be more complicated and often do not rotate as cleanly as the corresponding long periods. Thus, we emphasize the long-period data in this presentation.

Fig. 6 shows an enlargement of the data from Fig. 1. The arrival between *S* and *ScS* is particularly clear from 78° to 80°, where the direct *S* downswing shows an additional arrival, *Scd*, not apparent in the direct *S* pulse at closer distances. This interference shifts systematically with distance. On the right is a profile of synthetics computed with the Cagniard de Hoop method for model SLHO (Fig. 2). No radiation pattern is included in the synthetics, but this is of little consequence because the *SH* radiation is very stable between *S* and *ScS*. In constructing these synthetics we have not attempted to include individual station receiver structures, since these are not well known. Fortunately, many of the important observations are recorded at East Coast stations which have particularly simple *SH* receiver structures (Lay & Helmberger 1981), so this does not appear to be a major problem. The simple, impulsive waveforms of this event and subsequent events discussed in this study are adequately reproduced by the point sources used in the modelling.

Since the direct *S* travel times and *ScS-S* differential times for all the data presented in this paper are very consistent with the JB model predictions, as demonstrated in Lay (1983), we used the JB model with an increased core radius of 3485 km as a starting model in the waveform modelling. We tried to find the minimum perturbations to this model that would reproduce the travel times and amplitudes of the *Scd* arrivals. The velocity structure above 2300 km depth was kept fixed so that direct *S* times, to a distance of around 82°, in model SLHO are the same as for the JB model. Since the final model, SLHO, oscillates around the starting JB model, as seen in Fig. 2, the *S* and *ScS-S* times are very close to the original JB times and, hence, provide a good fit to the observations. This modelling procedure was greatly simplified by using the generalized ray theory technique which provides a clear interpretation of any model perturbations. The source wavelet used in the synthetics was determined by fitting a point source synthetic to the direct *S* observations in the range of 60–70° for each event.

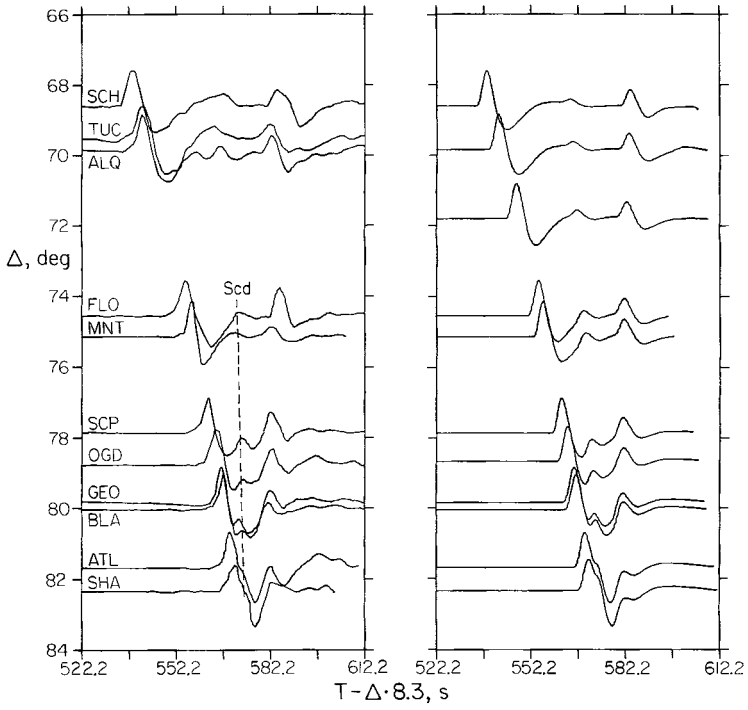

Figure 6. Observed (left) and synthetic (right) profiles of long-period *SH* seismograms for the event of 1970 September 5, (d = 583 km). The JB station residuals have been removed from the data and the amplitudes are normalized. The synthetics are for model SLHO.

In Fig. 6, the observed interference pattern between the direct *S* and *Scd* phases is closely matched in the synthetics. This interference pattern is sensitive to the depth and size of the discontinuity in model SLHO, and quite good resolution of the model parameters can be obtained when a range of source depths is considered.

In order to confidently interpret the *Scd* arrival it is clearly necessary to inspect and model many events. The possibility of systematic receiver structure effects, multiple source complexity, source region complexity, and contamination due to *SKS* or other phases must be considered. Since model SLHO constitutes a dramatic departure from previous lower mantle shear velocity models, we present additional data and synthetic comparisons for five other Sea of Okhotsk events at different source depths. The other four events analysed in detail, as well as less complete data sets for several additional events, are very consistent with the data shown here, but are essentially redundant because they are at similar depths to one of the events shown in this paper.

The *SH* data and synthetics for an intermediate depth event (d = 136 km) are shown in Fig. 7. For this source depth *sS* follows *S* by about 60 s. This phase is omitted from the synthetics. The *Scd* arrival is clearly apparent in the downswing of the direct *S* phase and model SLHO again reproduces the interference accurately. Close inspection of the traces shows that for both the observations and synthetics, *ScS* and *Scd* are shifted 5 s later relative to *S* than for the deep focus event in Fig. 6. Many of the stations used are different, but none of the available data have been omitted except when the traces overlap and the waveforms are very similar. The fact that the ray parameter for *Scd* is intermediate between those of direct *S* and *ScS*, as well as the systematic shift with source depth gives strong support to the interpretation of *Scd* as a lower mantle phase.

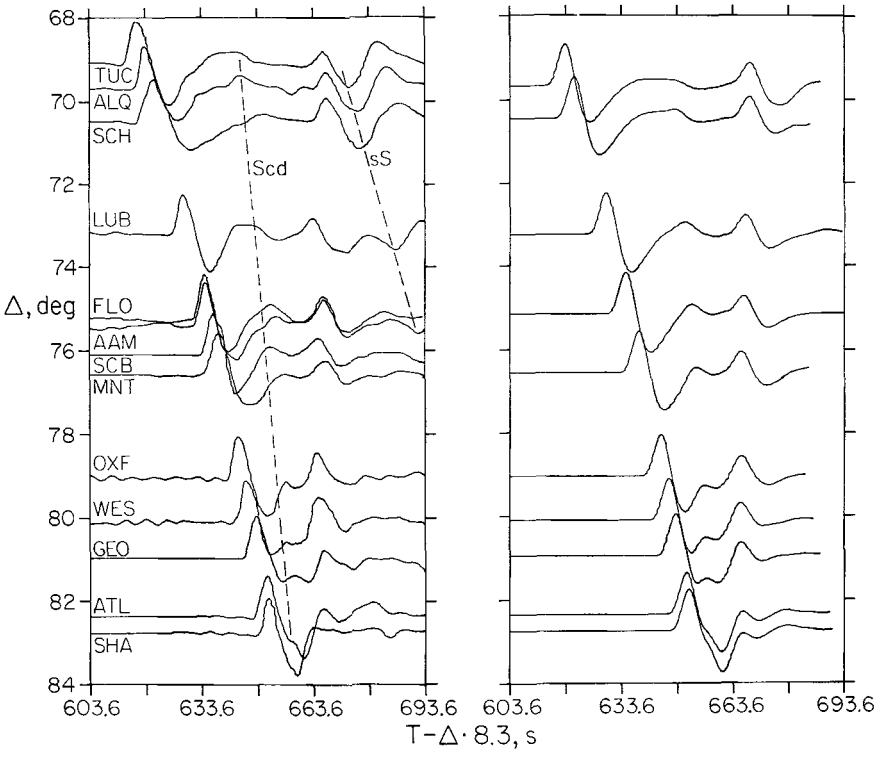

Figure 7. Observed (left) and synthetic (right) profiles of long period seismograms for the event of 1967 December 1. The source depth is shallow enough ($d = 136$ km) that *sS* can be observed in the data about 60 s after *S*. The JB station residuals have been removed from the data and the amplitudes are normalized. Note the interference in the downswing of *S* due to the *Scd* arrival. The synthetics are for model SLHO.

Fig. 8 shows data for an event at 402 km depth which is recorded out to slightly greater distances. The observation at BLA is very close to the crossover distance for the triplication in model SLHO. Note the high-frequency, large first pulse of this signal compared with those at SCP and DAL. This is clearly apparent in the synthetics at these distances. *Scd* becomes indistinguishable for distances less than about 72°.

Generally the short-period *SH* sections are too noisy to interpret; the observed signals are often very small and the profiles are sparse. One of the better quality short period sections ($d = 424$ km) is shown in Fig. 9 along with short-period synthetics for model SLHO. While there is certainly a large amount of scatter in relative amplitudes and significant *SH* coda, it is possible to identify *S*, *ScS* and *Scd* in all of the traces. Strong *Scd* arrivals are apparent at GEO, ATL and SHA, where model SLHO predicts that *Scd* is larger than *ScS*. The source wavelet in the synthetics was taken from the *S*-wave at GSC which is near 65°. The short-period synthetics show that *Scd* should be observable back to at least 72°, but the typical coda amplitudes in the short-period traces are comparable in size to the predicted *Scd* amplitude, so it is difficult to pick the arrival confidently. The observations at AAM and LUB do show arrivals of the appropriate size, but the waveforms are rather variable, as is true of the *ScS* waveforms.

The long-period records from the same event are shown in Fig. 10. These waveforms are somewhat more straightforward to interpret, particularly the strong interference at ATL,

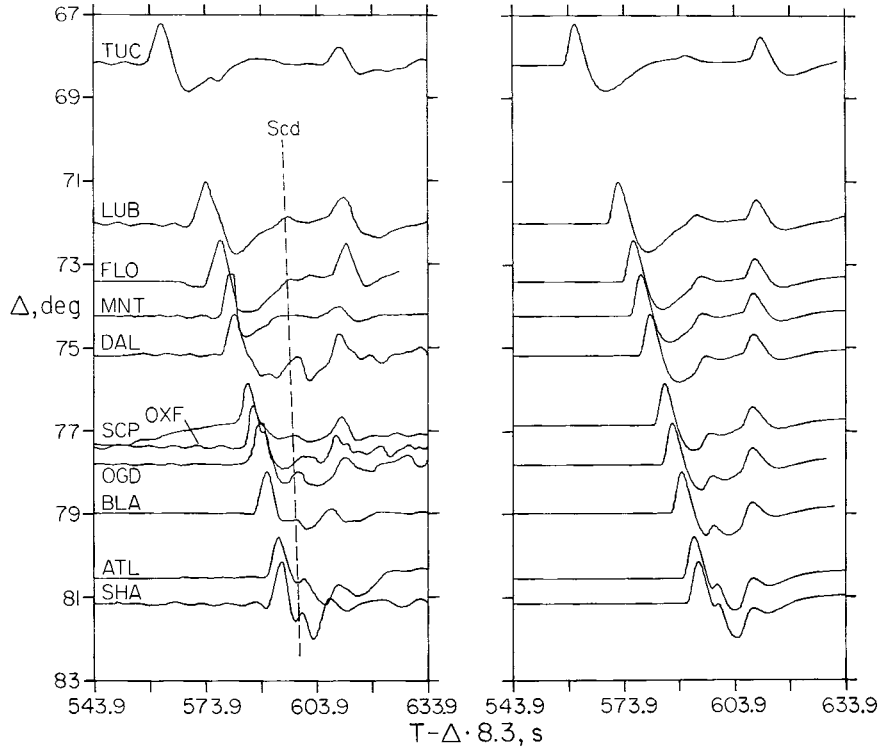

Figure 10. Observed (left) and synthetic (right) profiles of long-period *SH* seismograms for the event of 1964 March 18 ($d = 424$ km). The JB station residuals have been removed from the data and the amplitudes are normalized. The synthetics are for model SLHO.

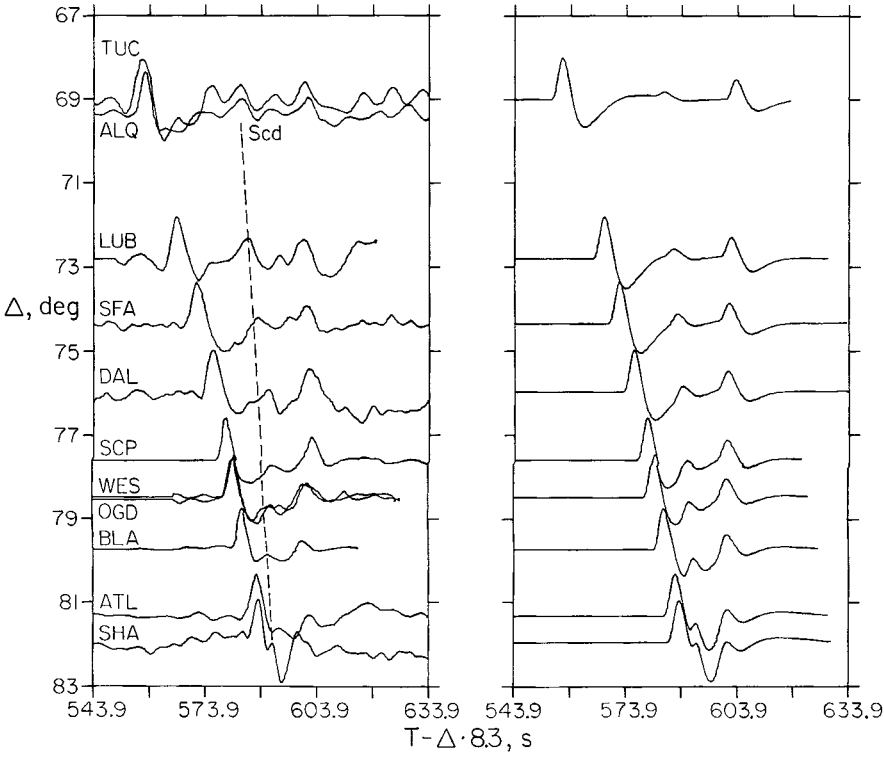

Figure 11. Observed (left) and synthetic (right) profiles of long-period *SH* seismograms for the event of 1967 October 12 ($d = 466$ km). The JB station residuals have been removed from the data and the amplitudes are normalized. The synthetics are for model SLHO.

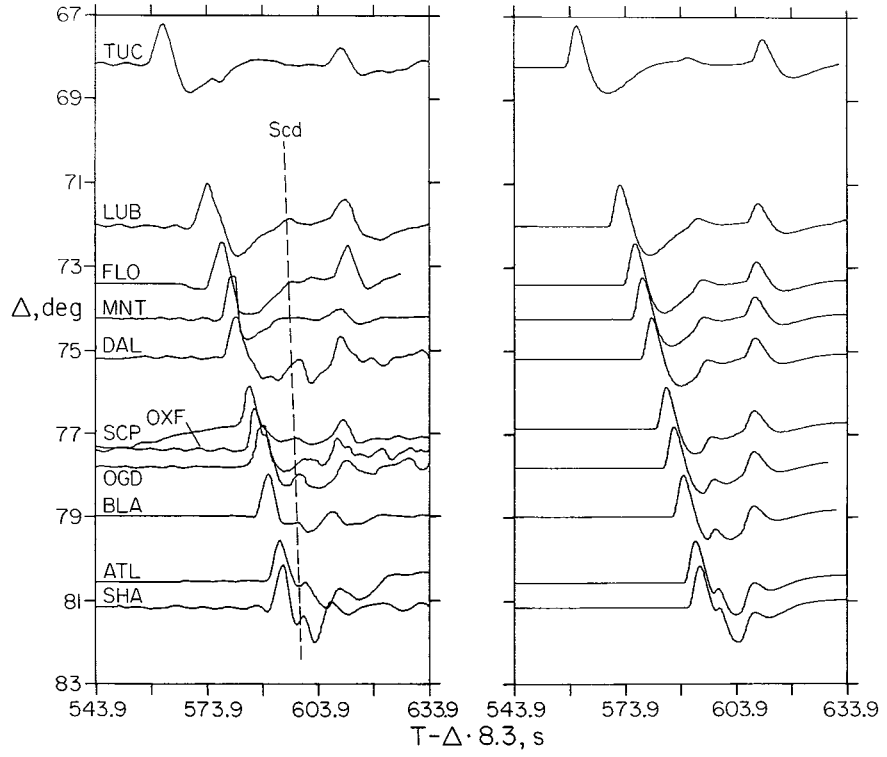

Figure 10. Observed (left) and synthetic (right) profiles of long-period *SH* seismograms for the event of 1964 March 18 ($d = 424$ km). The JB station residuals have been removed from the data and the amplitudes are normalized. The synthetics are for model SLHO.

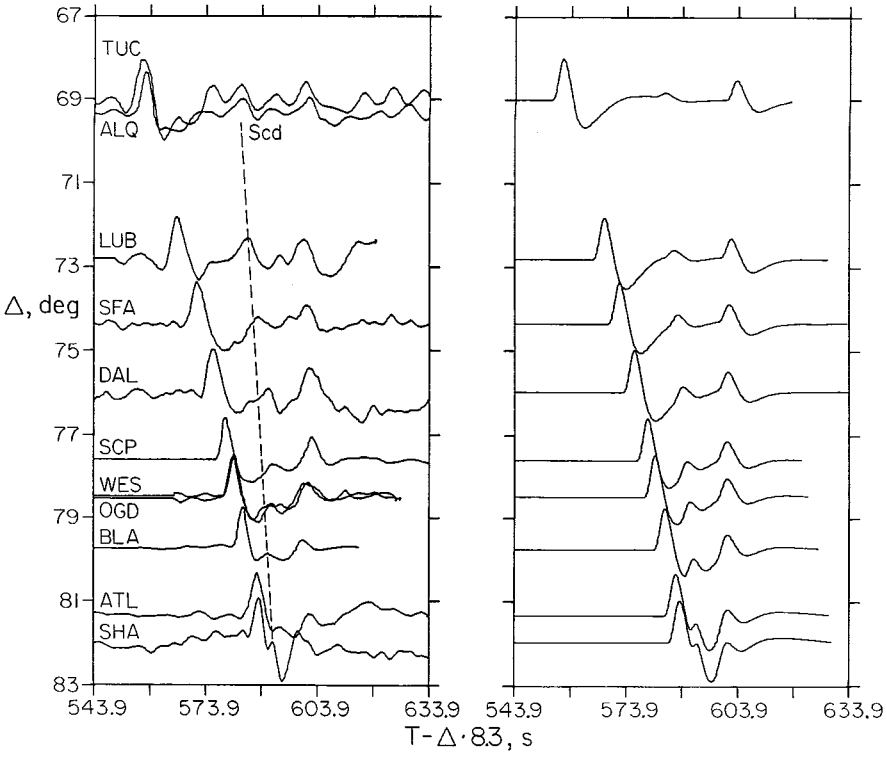

Figure 11. Observed (left) and synthetic (right) profiles of long-period *SH* seismograms for the event of 1967 October 12 ($d = 466$ km). The JB station residuals have been removed from the data and the amplitudes are normalized. The synthetics are for model SLHO.

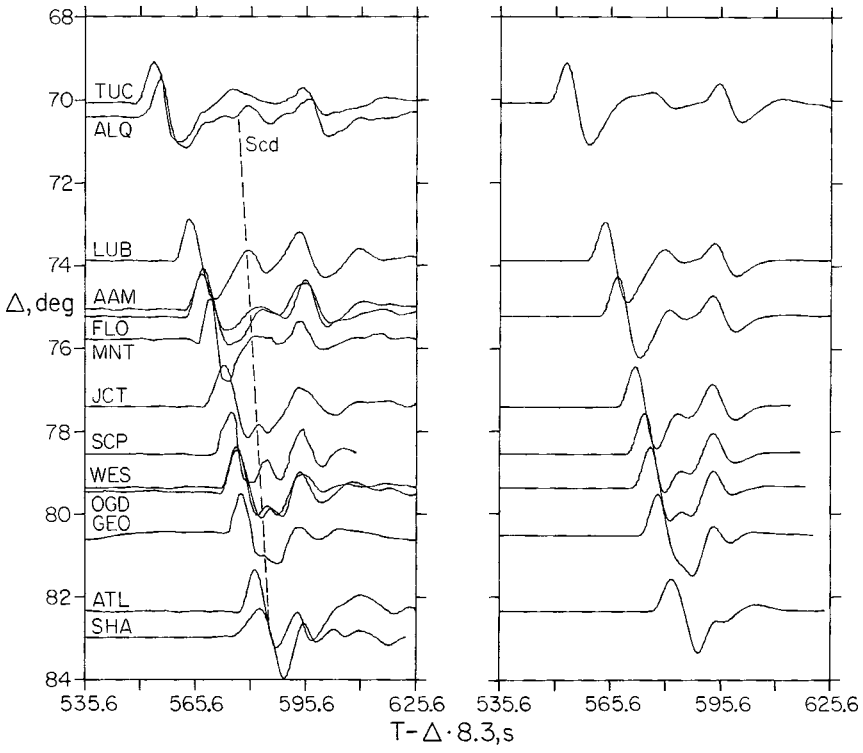

Figure 12. Observed (left) and synthetic (right) profiles of long-period *SH* seismograms for the event of 1971 January 29 (d = 540 km). The JB station residuals have been removed from the data and the amplitudes are normalized. The synthetics are for model SLHO.

SHA and BLA. The observation at LUB is well-modelled suggesting that the short-period observations are actually *Scd* on the near end of the triplication. A similar event (d = 466 km) is shown in Fig. 11. The *Scd* arrival is clearly observed. A profile for a deeper event (d = 540 km) is shown in Fig. 12. This event has a slightly longer source process than the others, but shows the *Scd* arrival from 74° to 82°.

A large data set of stable rotated *SH* signals is needed to identify the *Scd* arrival. Thus, it is not surprising that such a phase has not been previously reported, since few detailed *SH* waveform studies have been conducted. The interference of direct *S* and *Scd* on the long-period records makes it difficult to time the arrival of *Scd* accurately in order to invert the travel times for structure. We have attempted to avoid this difficulty by measuring the peak-to-peak differential times *ScS-S* and *Scd-S* for both data and synthetics in order to incorporate the travel-time information in the modelling process. Picking the peak of the *Scd* arrival on long periods produces fine structure in the differential times, for at distances greater than 75° this interference peak is dependent upon the source frequency content and distance. Fortunately, picking the same peak in the synthetics accounts for the interference effects. The differential travel-time data for events near six different source depths are compared with model SLHO times in Fig. 13. Given the nature of the travel-time picks, these plots actually provide an estimate of the waveform agreement between SLHO synthetics and the data. At a given distance there may be several seconds of scatter in both *ScS-S* and *Scd-S*, part of which is due to combining several events with different frequency content, and part of which is due to azimuthal variations in the differential times. Model

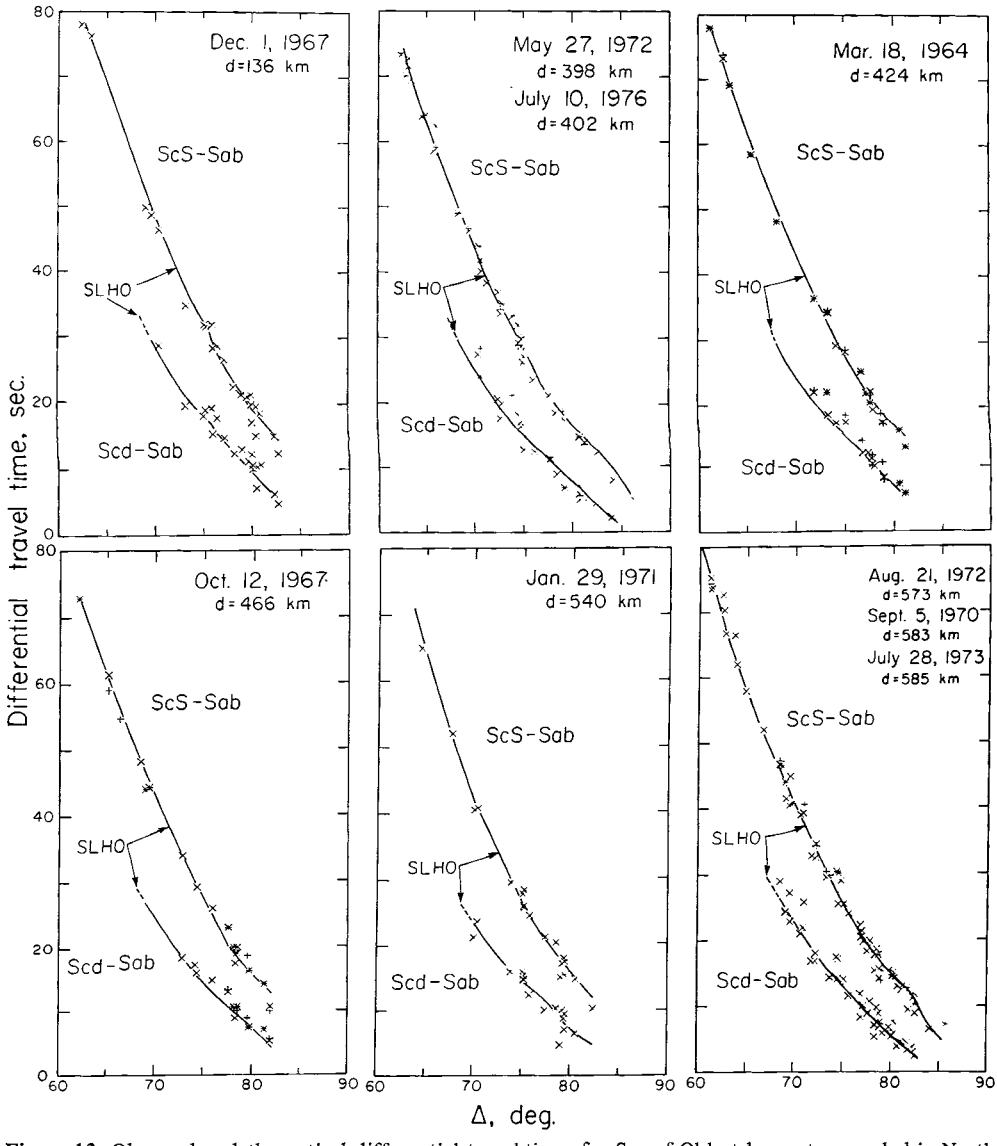

Figure 13. Observed and theoretical differential travel times for Sea of Okhotsk events recorded in North America. The travel times are measured from peak-to-peak for both short-period (+) and long-period (X) observations. The theoretical times are similarly measured from the synthetic seismograms. The *Scd* branch has very low amplitude at distances less than 70°.

SLHO does an excellent job of fitting both *ScS-S* and *Scd-S* at each source depth. The shift in differential times with source depth is clearly apparent in both the data and the model. The systematic behaviour of the *Scd* arrival for numerous sources of different frequency content, depth and distance indicates that it cannot be explained as a source complexity feature, nor as a near source multipathing phenomenon.

A surface focus geometric travel-time curve for model SLHO is shown in Fig. 14. The crossover distance is near 89° for a surface focus and shifts to near 85° for a 600 km deep event. This shift in the triplication position at a given range provides a means for eliminating receiver structure as a possible explanation of the *Scd* observations, since any receiver

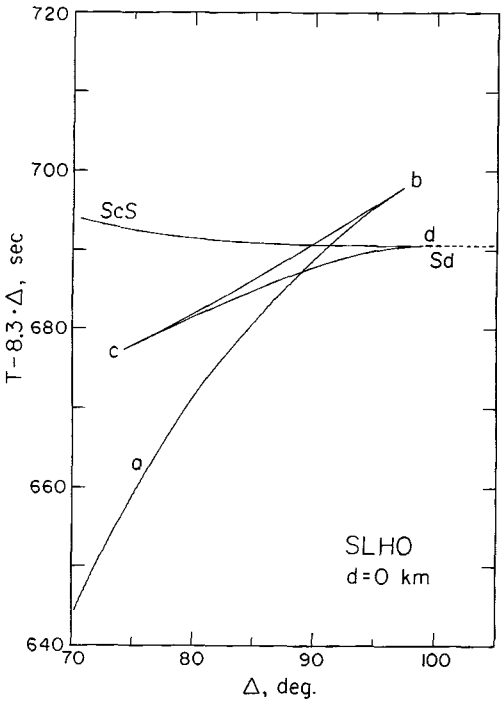

Figure 14. Geometric travel-time curve for model SLHO for a surface focus. The crossover distance shifts to 85° for a focal depth of 600 km.

complexities should be only weakly range dependent. Some comparisons of observations at a given station for several events of varying depth and distance are presented in Fig. 15, for four stations spanning different distance ranges from the Sea of Okhotsk events. The phases are aligned on the direct *S* arrival, and any systematic receiver phases should have a nearly constant time separation from the *S* arrival. At ALQ such an arrival can be seen 25 s behind *S*. This arrival interferes with *ScS* near 74° and could be mistakenly identified as *Scd* at 70°. Generally we have not found evidence for such large amplitude, late receiver phases (possibly *SH* reflections off the Moho). LUB, SCP and SHA show instances where *Scd* and *ScS* clearly have similar move out relative to *S*, which cannot be explained by receiver structure. Such comparisons have been made for all of the stations used in this study, along with comparisons of data from distinct source regions at a given station. The relative simplicity of the East Coast receiver structures has been confirmed by this procedure.

Only one other WWSSN station outside of North America lies along the same azimuth from the Sea of Okhotsk at slightly greater distance. This is BEC (Fig. 4), which ranges from 85° to 91° from the events used. For model SLHO this is in the range from crossover distance to just beyond, where *Scd* is predicted to become a first arrival. This crossover phenomenon is readily apparent at BEC as shown in Fig. 16. The synthetics are computed for the appropriate distances and source depths. The simple waveform near 86° is produced by constructive interference of *Sab*, *Scd* and *ScS*, all arriving essentially within the first upswing. For a shallow event such as that of 1974 September 21, the crossover is expected to shift to a somewhat larger distance, hence the observation at 88° is similar to that near 86° for the deeper source. However, a few degrees beyond crossover, near 90°, the arrivals separate by enough to broaden the first upswing. There is also a dramatic change in the ratio

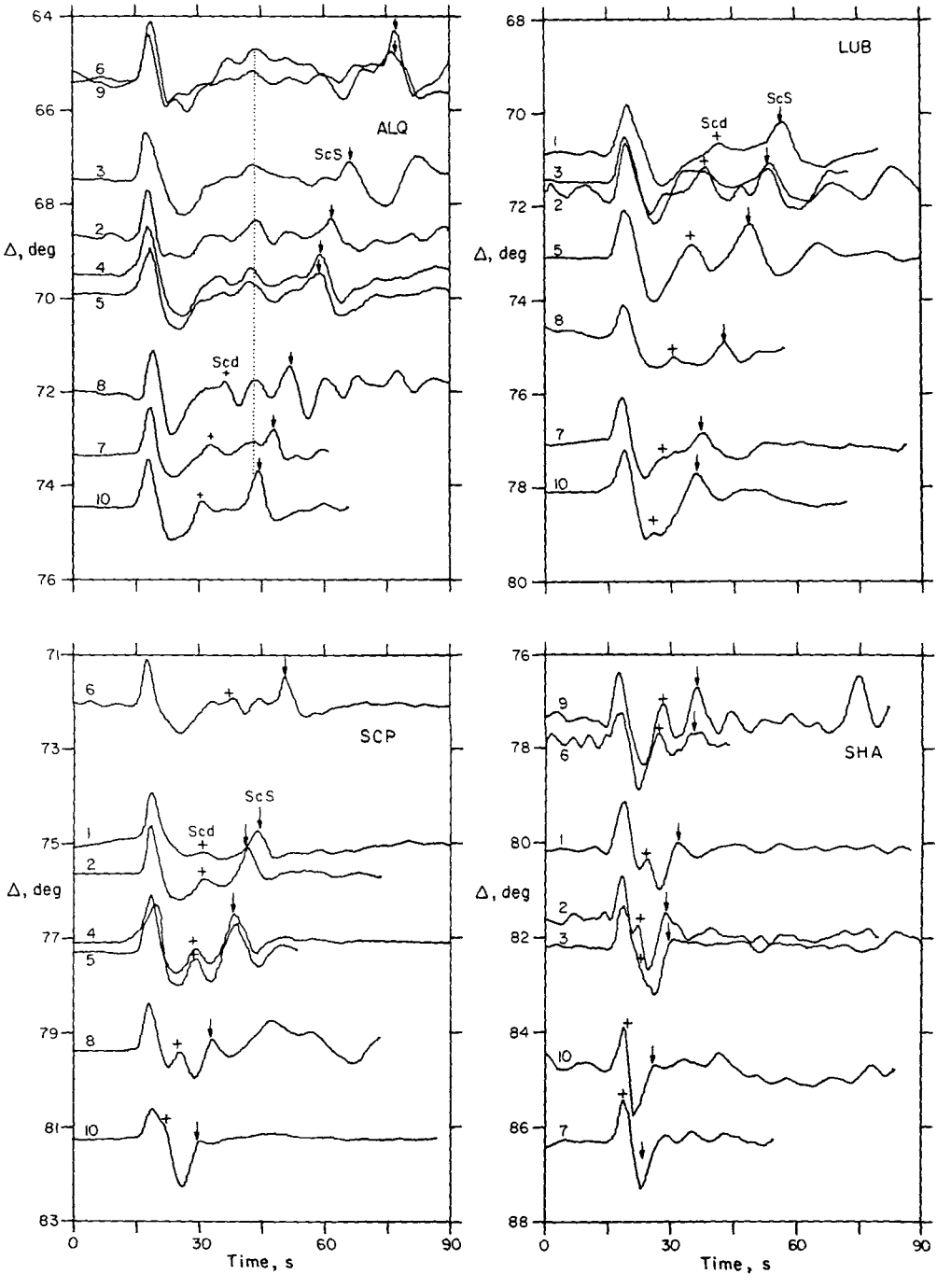

Figure 15. Comparison of *SH* recordings from several Sea of Okhotsk events at individual stations. The possible *Scd* arrivals are indicated by a (+) and *ScS* by (↓). The numbers indicate the event in Table 1 corresponding to each trace. The traces are aligned on the *S*-wave arrival. The distance at which each observation is plotted is such that the observed *ScS*–*S* time is the same as predicted for the JB model at that distance for a focal depth of 600 km. For station ALQ the dotted line indicates an arrival which is observed at the same time relative to *S* for all events, which is interpreted as a receiver phase. Note that *Scd* cannot be due to receiver structure and is difficult to observe closer than 71°.

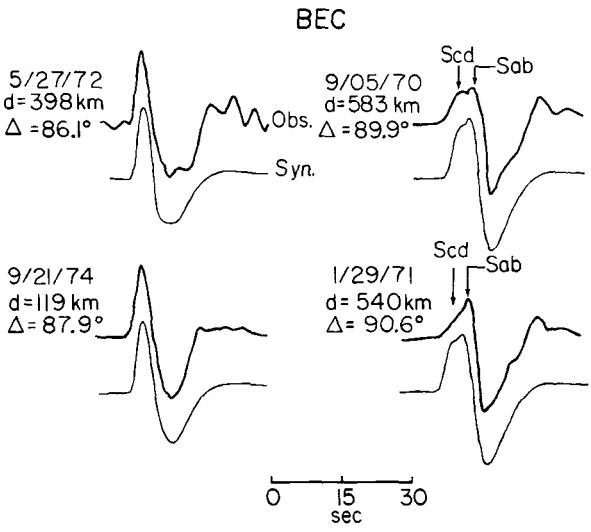

Figure 16. Observations and synthetics of *SH* records at BEC for several Sea of Okhotsk events. As the distance increases from 86°, which is near crossover distance, to 90°, the interference between *Scd* and *Sab* becomes apparent. The synthetics are for model SLHO.

of upswing to downswing amplitudes. This behaviour is very consistent with the model SLHO, and the waveform distortion is unlike that observed in any of the direct *S* phases at closer distances.

Since the tests described above fail to explain *Scd* as a source region or receiver phase, and the data are very consistent with the predictions of a lower mantle discontinuity, it appears that model SLHO is an appropriate velocity structure for the lower mantle between the Sea of Okhotsk and North America. The waveform information places rather tight constraints on the permissible velocity model. The velocity discontinuity is constrained in depth to 278 ± 25 km above the CMB, and the velocity increase is 2.75 ± 0.25 per cent. The observations near 90° are particularly sensitive to the velocity contrast across the discontinuity. The direct *Sab* arrival has the same travel times as the direct *S*-wave for the JB model to distances near 80°, and becomes several seconds later than JB between 80 and 89°, as is observed in recent *S*-wave travel-time studies. The velocity gradient above the discontinuity in SLHO is probably somewhat steeper than necessary if the JB velocity structure were tapered off at shallower depth. This does not strongly affect the waveform modelling process. Beyond 100° diffracted *Sd* becomes the only significant arrival.

In an attempt to constrain the velocity gradient below the discontinuity, we compared the amplitudes of *ScS* with direct *SH* in the distance range 40–80°. Mitchell & Helmberger (1973) suggested that the *ScSH/SH* amplitude ratio can be used to constrain the shear velocity gradient just above the core. We measured the peak-to-peak amplitude ratios for the Sea of Okhotsk observations, corrected them for radiation pattern using the mechanisms in Table 2, and plotted them as a function of distance as shown in Fig. 17. There is a fair amount of scatter, but the observations are numerous enough to define the mean amplitude ratio in each 5° increment of distance. The amplitude ratios for *SH* synthetics for the JB model and SLHO are also shown in Fig. 17. Both models are in good agreement with the observations, indicating that smooth positive or near zero velocity gradients within D″ are consistent with the Sea of Okhotsk data. However, it turns out that the *SH* amplitude ratios are not particularly sensitive to the shear velocity gradient in D″, as discussed in Lay & Helmberger (1983).

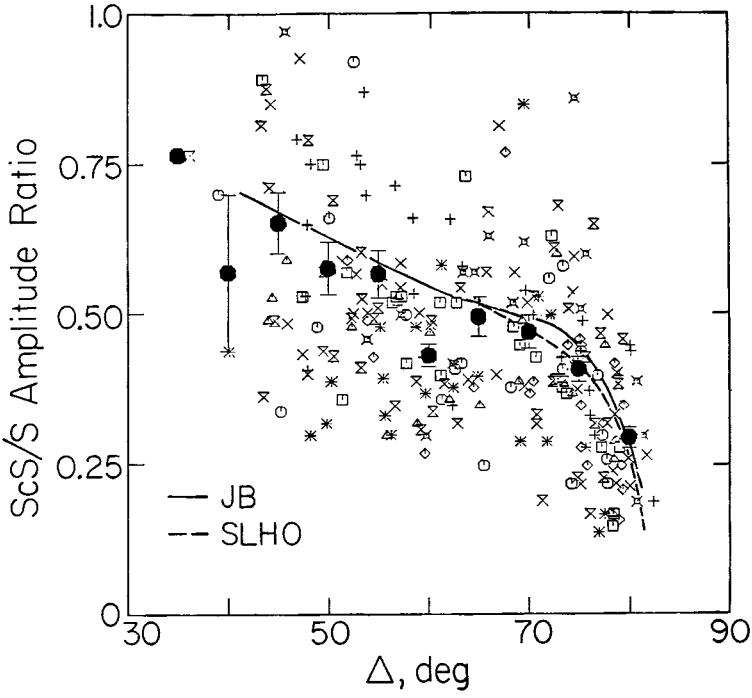

Figure 17. The long-period *ScS/S* amplitude ratio for Sea of Okhotsk observations in North America. Different symbols correspond to different events. The amplitudes are measured peak-to-peak for both data and models. The solid symbols give the mean and standard error of the observations in each 5° increment of distance. At distances greater than 75° the amplitude ratio is contaminated by interference between *S* and *ScS*.

The sharpness of the velocity discontinuity is an important feature to resolve, but the long-period records yield little constraint on this. The short-period data are not easy to interpret, but we can an least make some consistency arguments for a rather sharp velocity discontinuity. Fig. 18 shows several variations of model SLHO where the velocity jump is replaced by transition zones of varying thickness. Long-period synthetics throughout the triplication range are indistinguishable for these models, but short-period synthetics on the near end of the triplication (near the C cusp) do show substantial differences. Fig. 19 compares a typical short-period observation at 73.4° with short-period synthetics for SLHO and the transition zone models. Using the ratio of the amplitudes in the time window for *Scd* and *ScS* as a guide, it is clear that the data are compatible with a sharp increase. It is also apparent that a transition zone 45 km thick or thicker does not produce a large enough short-period *Scd* arrival. Other short-period data yield a similar conclusion.

The modelling procedure employed above does rely on rather subjective quality of fit assessment and it would be attractive to employ an inversion procedure that could more quantitatively span the model solution space. One of the major obstacles to applying a waveform inversion analysis to the *SH* data is that large travel-time anomalies exist in the data, indicative of lateral variations in the mantle that are not easily incorporated in any automated modelling procedure. Examples of the azimuthal variations are shown in Fig. 20. The signals are recorded at the same distance from each event at stations separated by less than 20° in azimuth. Note that with the traces aligned on the *ScS* arrival, the *Scd* arrivals are at the same relative time, but the relative timing of *Sab* can vary by 4.4 s. Such data indicate that the azimuthal variations affect the direct *S*-waves more strongly. This could be due to

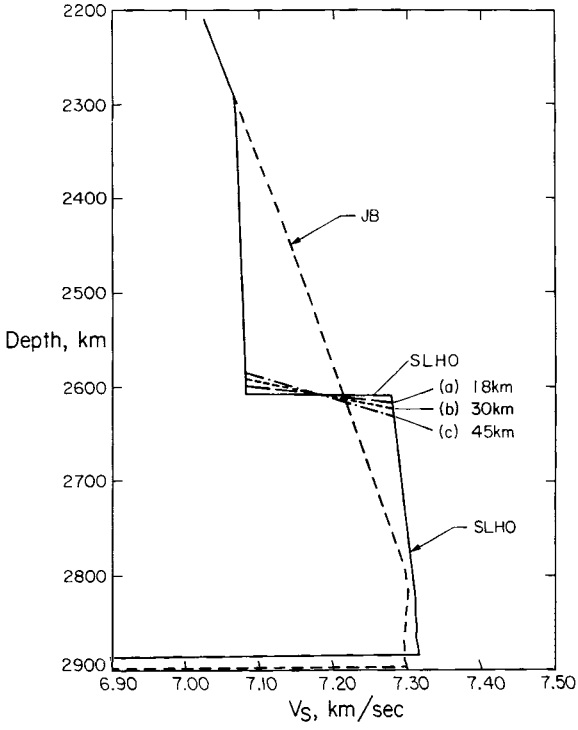

Figure 18. Perturbations of model SLHO where the velocity discontinuity is replaced by transition zones of various thicknesses.

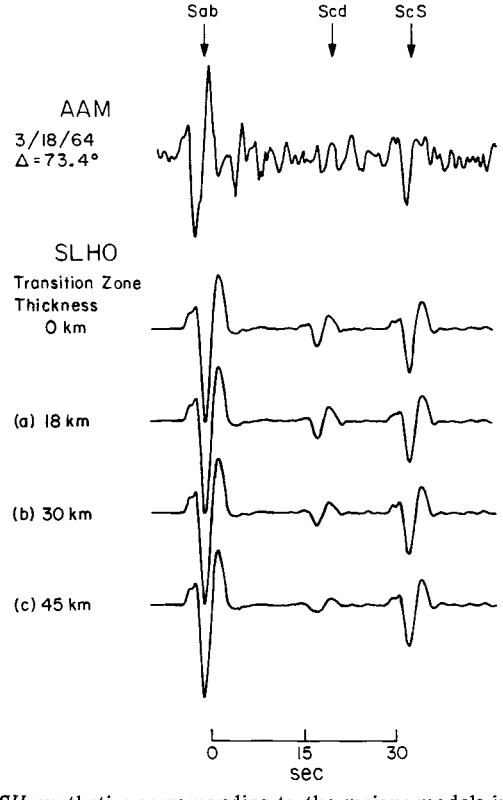

Figure 19. Short-period *SH* synthetics corresponding to the various models in Fig. 18. A typical observation on the near end of the triplication is shown at the top. Long-period synthetics for the corresponding models are indistinguishable.

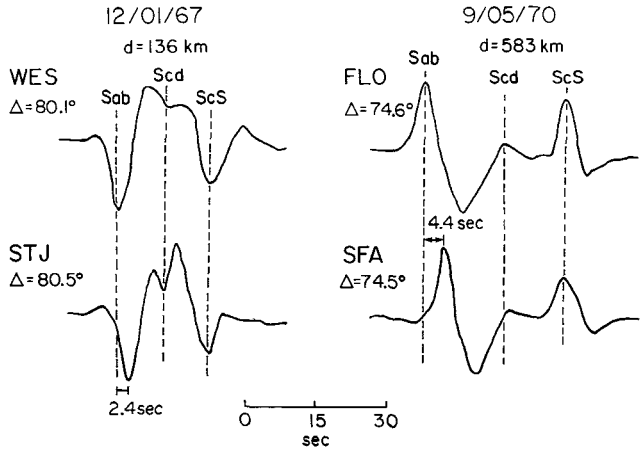

Figure 20. Representative *SH* signals indicating the azimuthal travel time effects in the data. The *ScS–S* differential times at a given distance can vary by as much as 6 s. The *ScS–Scd* times tend to vary less, though the nature of the *Scd* arrival at these distances is affected by the timing of *Sab*, as in the WES–STJ comparison. The azimuth differences are 10° for WES and STJ and 17° for FLO and SFA.

either a near source anomaly, such as that proposed for the Sea of Okhotsk deep source region by Jordan (1977) or an anomaly along the Sab path in the mantle several hundred kilometres above the D″ region, such as proposed for South American data in Lay (1983). These large differential time anomalies clearly affect the nature of the *Scd* arrival at distances near 80°, where it interferes with *Sab*, and this is difficult to allow for in any waveform inversion scheme. The stability of the *ScS–Scd* differential times suggests relative homogeneity of the lowermost 400 km of the mantle in the region sampled by the Okhotsk data.

Model SLHO is consistent with all of the Sea of Okhotsk *SH* data observed in North America, but the question arises as to whether the *SV* data are compatible with this model. *SH* waveform modelling alone cannot distinguish both shear velocity and density changes, so it is desirable to examine *SV* data in order to place any additional constraints on the density behaviour across the D″ discontinuity. The major problem with *SV* data is that if large amplitude, stable *SV* and *ScSV* pulses are observed, there will also be large *SKS* phases. This is demonstrated clearly by a profile of *SV* signals for the event of 1970 September 5, shown in Fig. 21. The *SKS* arrival is the strong upward pulse that sweeps through the *SV* signal, crossing over it near 81°. Note that *ScSV* has opposite polarity to direct *SV*, while one would expect the *SVcd* arrival for model SLHO to have the same polarity as *SVab* in this distance range. While there is some hint of the *SVcd* arrival at FLO, MNT and SCP, the *SKS* arrival crosses right through the time window of interest, making it practically impossible to look for the discontinuity in the *SV* data.

Since the model derived for the Okhotsk data involves a major Earth structure feature, we have checked the *SH* synthetics generated by the Cagniard de Hoop method by comparing them with the reflectivity method as developed by Fuchs & Müller (1971) and Kind & Müller (1975). This was done to ensure that the partial ray sum used in the ray theory modelling does not introduce spurious features in model SLHO. A comparison of synthetic *SH* profiles for the two methods is shown in Fig. 22. The source depth is 580 km and no Q structure is included. A relatively high-frequency source wavelet is used to enhance the waveform features. The reflectivity synthetics have a very slight radiation pattern in them. The generalized ray theory (GRT) and reflectivity synthetics for model SLHO are in

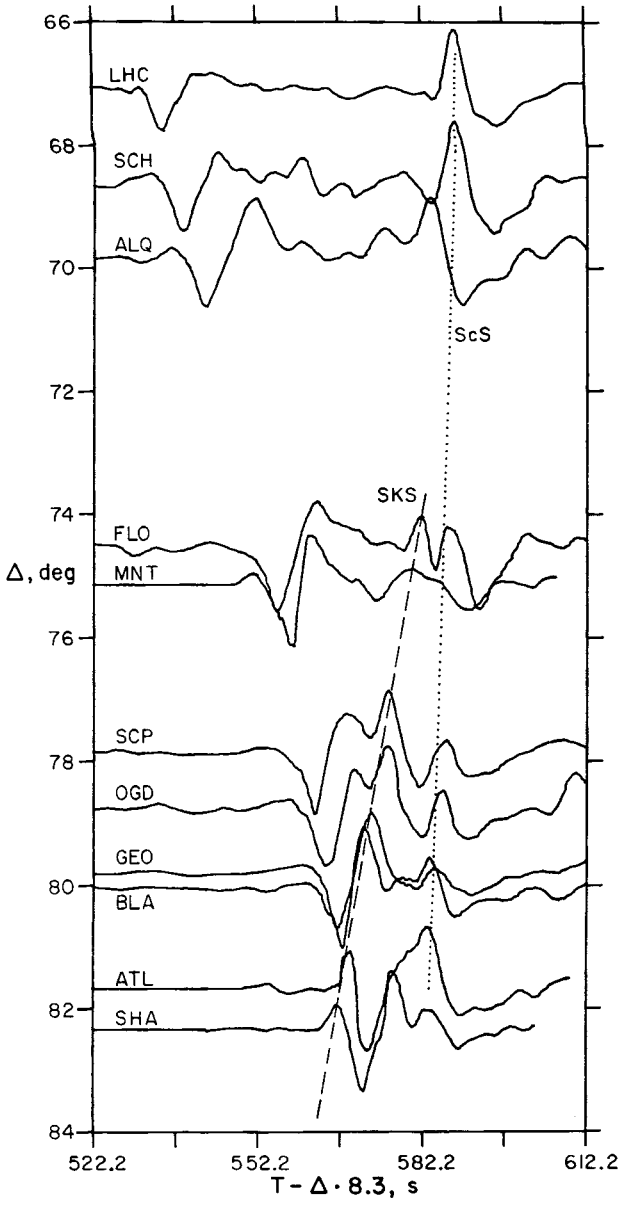

Figure 21. Profile of long-period radial component *SV* signals for the event of 1970 September 5, (d = 583 km). The corresponding *SH* seismograms are shown in Fig. 6. The JB station residuals have been removed from the data and the amplitudes are normalized. Note the reversal in polarity of the first arrival as SKS crosses the direct *S* arrival.

excellent agreement throughout the triplication, with the synthetics at 92.5° showing the largest deviation, which is minor. From this test it appears that the ray theory waveform modelling is adequate for this application.

Using the reflectivity program, we have computed the effects of the proposed D″ velocity structure on diffracted *SH*. A comparison of diffracted synthetics for the JB model and the Sea of Okhotsk model is shown in Fig. 23. The source wavelet has a dominant period of 20 s, which is comparable to long-period diffracted *SH* observations at WWSSN stations. In the

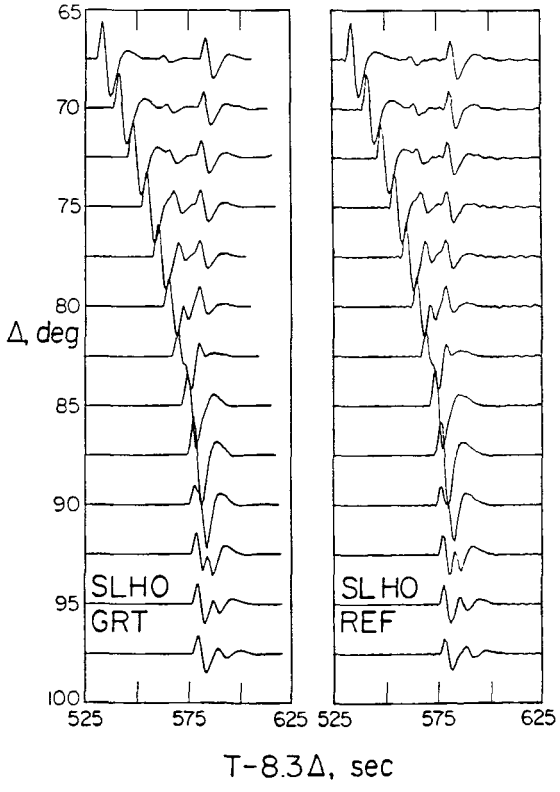

Figure 22. *SH synthetics computed with the Cagniard de Hoop generalized ray theory (GRT) technique and the reflectivity (REF) technique for the Sea of Okhotsk model. The agreement between these techniques throughout the entire range of the lower mantle triplication is clearly apparent.*

range 95–100° the *Sab* branch produces a secondary arrival which diminishes rather quickly. For model SLHO the amplitude decay into the core shadow is similar to that of the JB model. It is unlikely that diffracted *S* studies which have typically used data beyond 100° could distinguish between the SLHO and JB models, even in the absence of source and receiver noise. It may be possible to examine diffracted *S* traversing the same portion of D″ as sampled by the Sea of Okhotsk data to seek the subtle differences between these velocity models, as well as to further constrain the overall velocity gradient within D″.

Sea of Okhotsk data recorded in Europe

Having established the presence of the lower mantle *S*-wave triplication in the Sea of Okhotsk data recorded in North America, it becomes of interest to examine other source region–receiver combinations to determine whether the discontinuity is global and what lateral variations may accompany it. The distribution of long-period seismographs in North America is denser than anywhere else; however, a relatively dense array of WWSSN stations in Europe recorded the same Sea of Okhotsk events used above as well as other Sea of Japan events. Fig. 24 shows the epicentres and station distribution used for the European paths. A profile of *SH* seismograms across this array is shown in Fig. 25, for the event of 1970 September 5. Note the very simple signals and minimal receiver coda between *S* and *ScS*. This provides further evidence that this event, which was used extensively above, is not

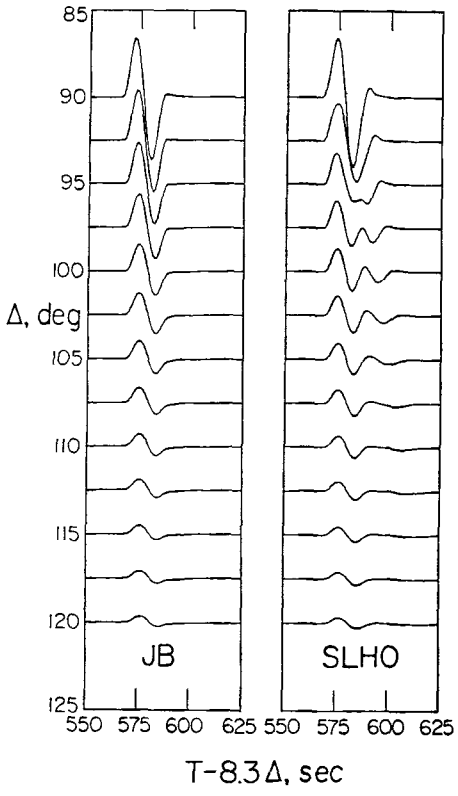

Figure 23. *SH* synthetics for the JB and Sea of Okhotsk models shown in Fig. 2. The reflectivity technique was used to compute the signals. The amplitude scale is the same for both models. The presence of the receding *Sab* branch causes the distortion in the range 95–100° for models SLHO. The diffracted signals, beyond 105°, are very similar for the two models, with little discernible difference in waveform character.

anomalous in its source complexity. Between 74° and 76° the *Scd* arrival appears to be present once again. The paths to these stations are very distinct from those to North America so this arrival appears to have a common lower mantle origin. Note that stations TOL and MAL near 90° show distortion of the first pulse similar to that seen at BEC, with broadened first pulses and small upswing to downswing amplitude ratios.

Another profile of data is shown in Fig. 26, with very similar features. The observations at VAL and TRI show the clearest evidence for the triplication, though, once again, MAL shows a split first pulse. Comparisons of the *SH* recordings at VAL and TRI for several events are made in Fig. 27. In neither case can the apparent *Scd* arrivals be explained as receiver phases or source complexity. Thus, despite the spareseness of the data it appears that the European data are consistent with the North American results. However, close inspection of the traces shows that the waveforms are slightly shifted relative to those in North America.

Observations near 75° in Canada, at stations SFA and MNT, are compared with the observations at VAL and TRI in Fig. 28. Synthetics for model SLHO are in close agreement with the Canadian observations as expected, but the *Scd* arrival is relatively late compared to the waveforms at VAL and TRI. This shift is several seconds and appears to be quite systematic. Moving the velocity discontinuity in SLHO upward by 40 km and keeping the

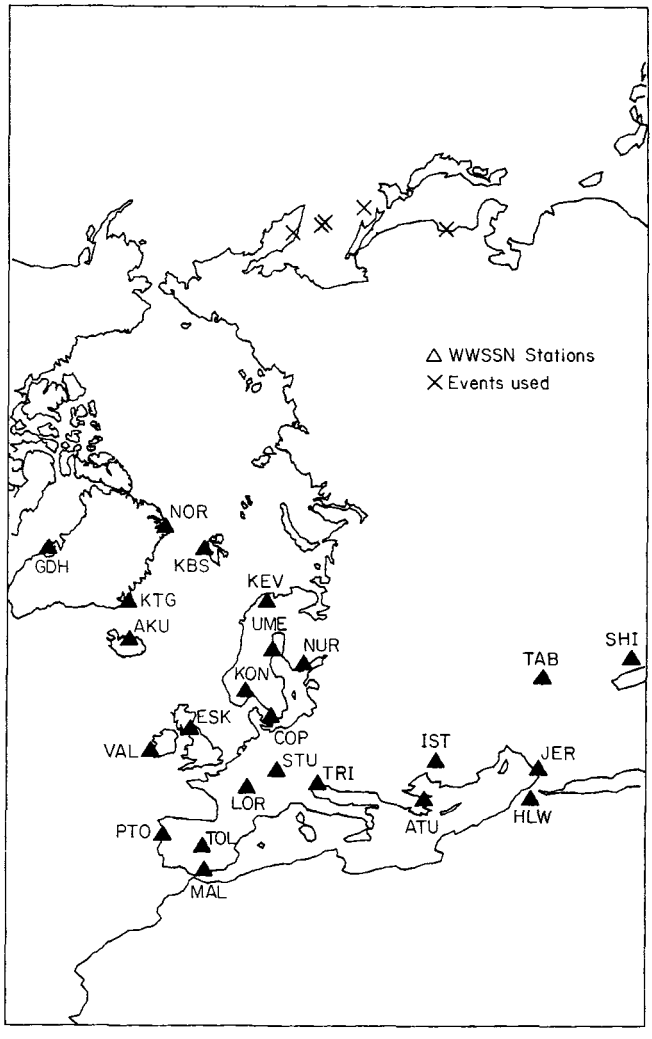

Figure 24. Azimuthal equidistant projection showing the location of Sea of Okhotsk and Sea of Japan epicentres and European WWSSN stations used in this study.

same 2.75 per cent velocity jump gives model SLHE, for which the *ScS–Scd* separation and *Scd* amplitude are in agreement with the European data. It is not possible to simply decrease the average D″ velocity enough to produce the several second *ScS–Scd* travel-time shift without having very strong negative velocity gradients. Thus, we feel that variation in the depth of discontinuity is the more reasonable explanation for this shift.

Argentine events recorded in North America

Deep focus Argentine earthquakes have suitable locations and mechanisms for examining the *SH* signals across North America. All short- and long-period *SH* seismograms recorded in North America were digitized and rotated for seven suitable deep focus events. No intermediate depth events with adequate location, size and orientation to seek the triplication were found in the data since 1963. The station distribution and epicentres are shown in

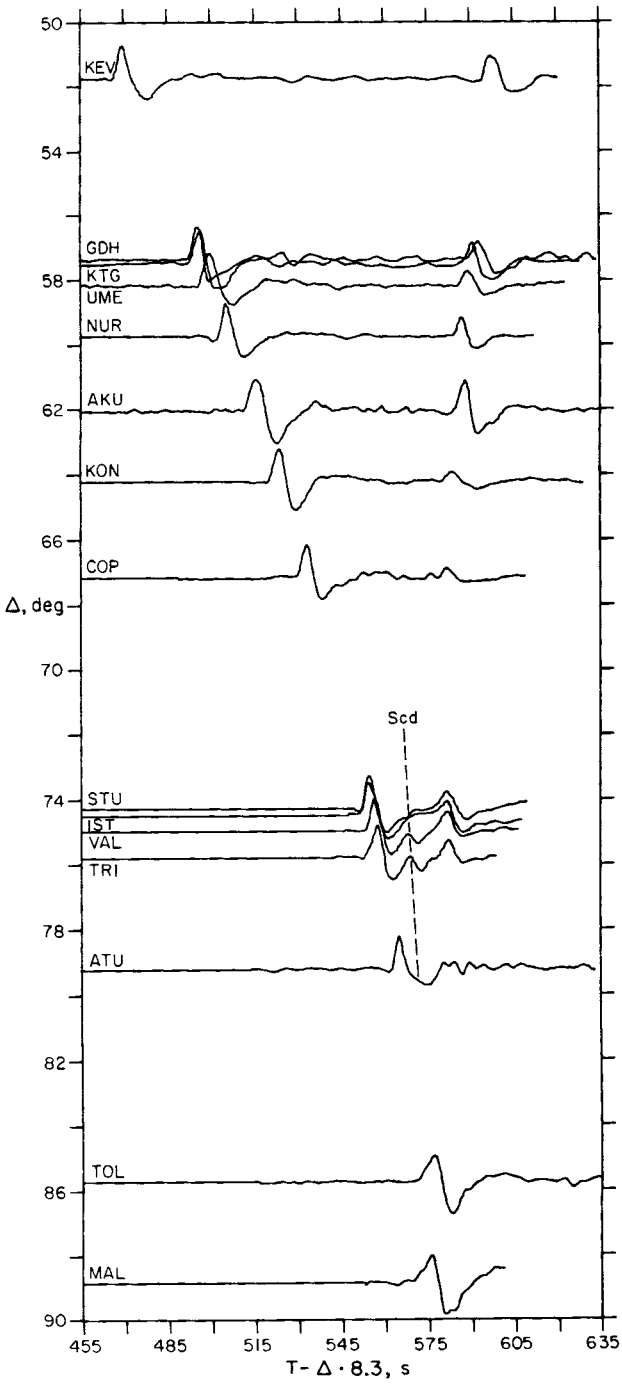

Figure 25. Profile of tangential components of European stations for the 1970 September 5, Sea of Okhotsk event (d = 583 km). Note the simple pulses similar to those in Figs 1 and 6, and the arrival of *Scd* apparent near 75° and in the distortion of the first upswing at TOL and MAL.

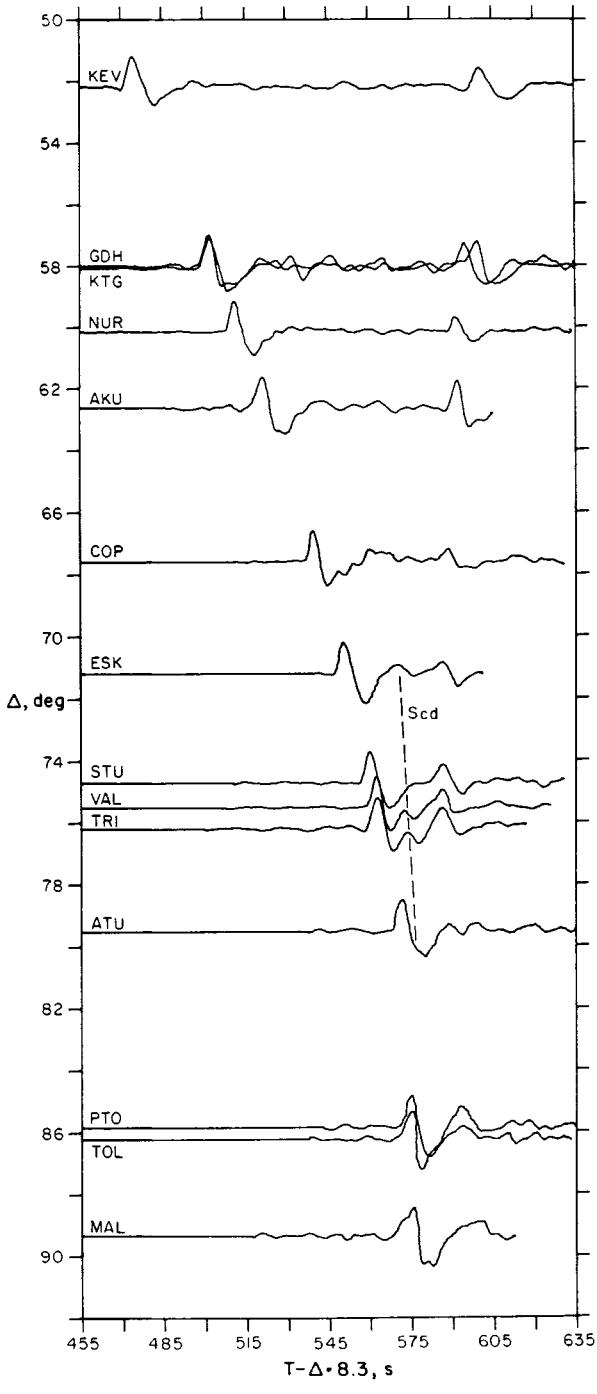

Figure 26. Profile of tangential components at European stations for the 1971 January 29, Sea of Okhotsk event ($d = 540$ km). Note the arrival of *Scd* near 75° and the distortion of the first pulse at MAL.

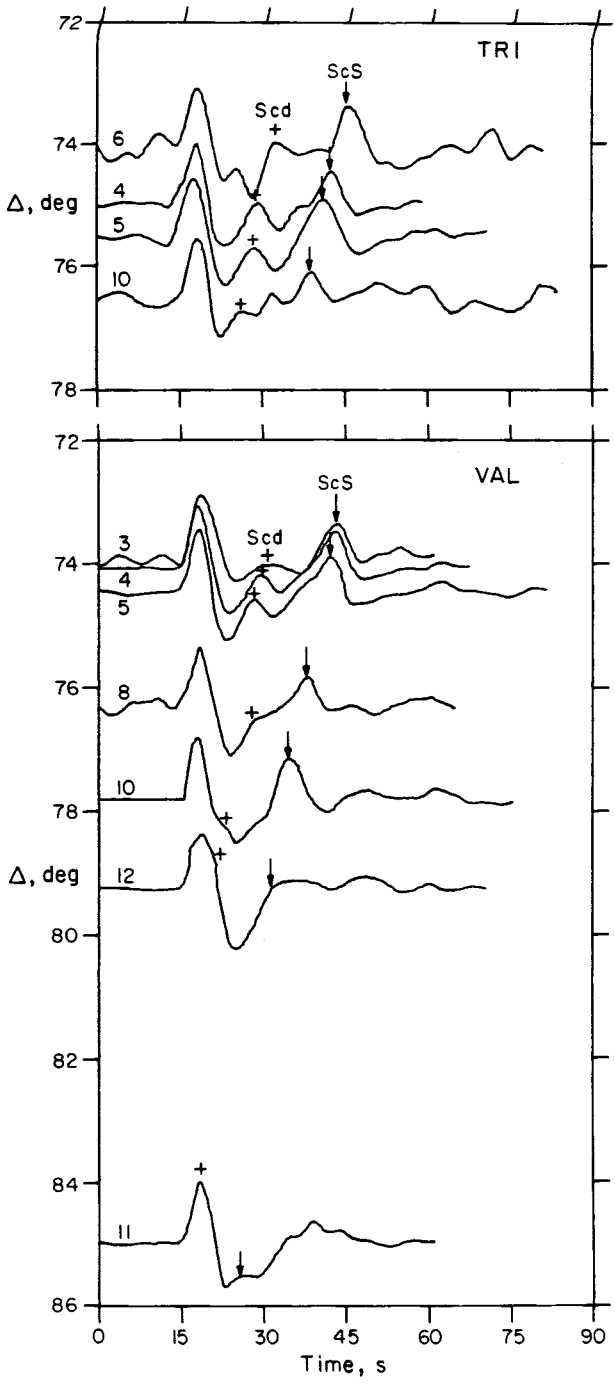

Figure 27. Comparison of *SH* observations at VAL and TRI for several Sea of Okhotsk and Sea of Japan events. The numbers indicate the event in Table 1 corresponding to each trace. The data are treated as in Fig. 15.

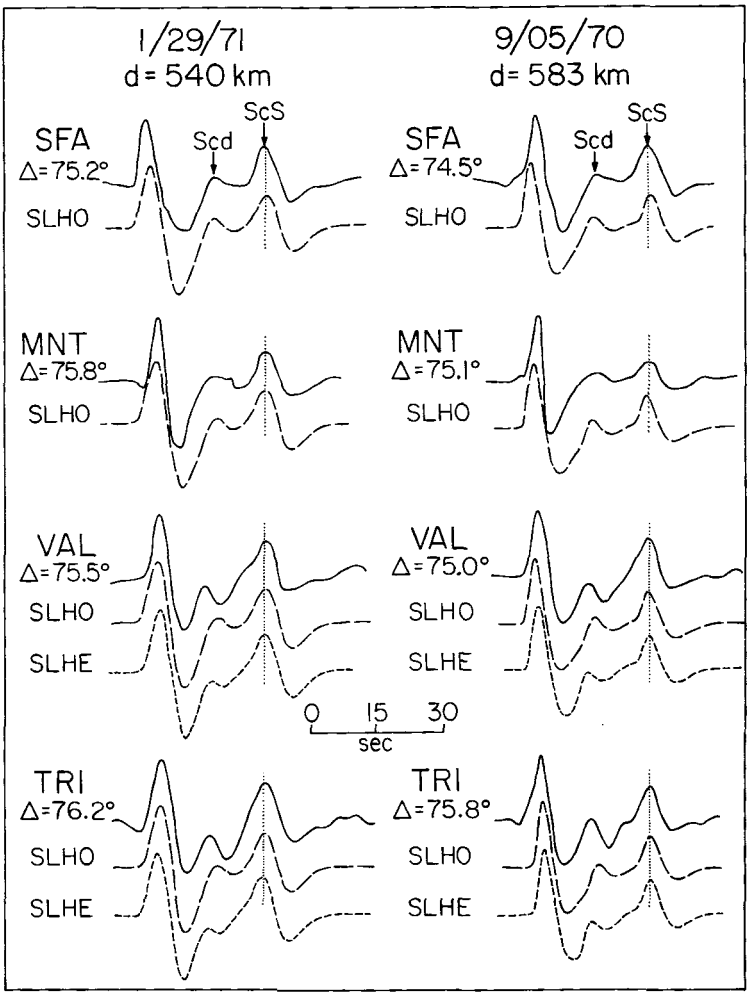

Figure 28. Comparison of observations and synthetics for two deep focus Sea of Okhotsk events. SFA and MNT are Canadian stations, and hence are well modelled by SLHO (derived for paths to North America from the Sea of Okhotsk). VAL and TRI are European stations, so the paths to these sample distinct lower mantle. The *Scd* arrival is clearly visible at these stations, but arrives earlier than in the Canadian data or model SLHO. Model SLHE is similar to SLHO except that the major discontinuity is 40 km shallower.

Fig. 29. The azimuthal travel-time anomalies in the Argentine data are particularly strong, with *ScS-S* residual variations of up to 8 s across the narrow azimuth range to North America. An attempt was made by Lay (1983) to isolate the cause of these azimuthal anomalies with the conclusion that the direct *S* phases encountered localized fast and slow regions in the mantle at depths of 1000–1900 km below the Caribbean and 1700–2700 km below northern Brazil and Venezuela, respectively. If this interpretation is correct, the *ScS–Scd* differential times for any lower mantle triplication should show less variation than the *ScS–Sab* differential times. Thus, in plotting the data profiles from Argentina we align all the traces on the *ScS* arrival and seek the *Scd* branch.

Fig. 30 shows the *SH* seismograms for the event of 1967 January 17, which is known to be a simple event (Lay & Helmberger 1981). It is clear that large *ScS–S* variations afflict

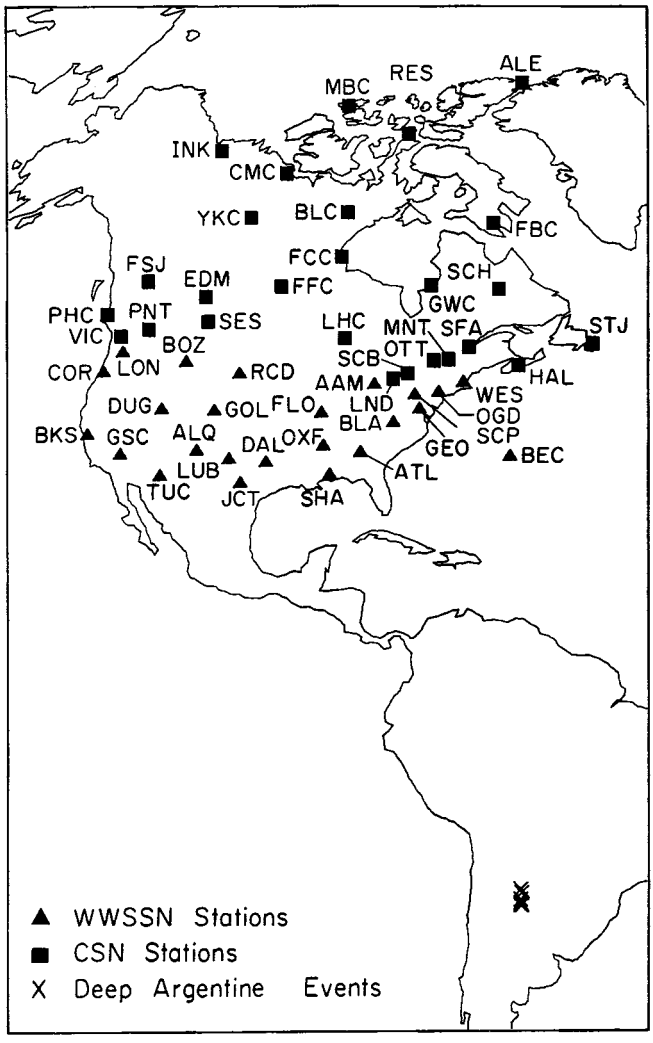

Figure 29. Azimuthal equidistant projection showing the location of deep Argentine event epicentres and North American stations. GSC, RCD and SCH are approximately 80° from the Argentine source region.

the data; however, given the alignment of *ScS* it proves possible to pick the *Scd* arrival in the range 71–81°. Note the difference in *ScS–Sab* times at ALQ and SFA, but the consistency in *Scs–Scd* at these two stations. PAS and GSC show strong interference in the downswing that is consistent with the *Scd* arrival. GOL and DUG are very long-period signals which show small *Scd* effects, but also comparably small *ScS* arrivals.

Another section aligned on the *ScS* arrival is shown in Fig. 31. The *Scd* branch can again be traced back to about 70°. A third section is shown in Fig. 32, with strong *Scd* arrivals at SFA, STJ, LHC and GSC. The other Argentine data profiles are similar, with fairly consistent *Scd* arrivals being apparent despite the large *ScS–Sab* travel-time anomalies. These data are not straightforward to model as the Okhotsk data, and not many stations lie in the range 75–80° where the *Scd* arrival should be strongest. However, the events have quite simple source characters and high signal-to-noise ratios.

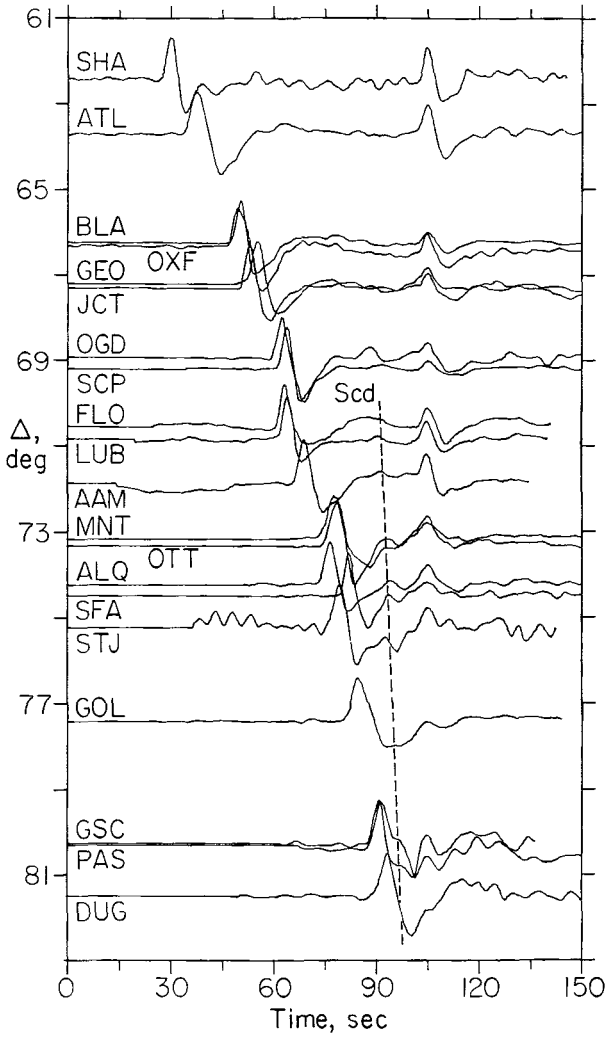

Figure 30. Profile of tangential component observations for the Argentine event of 1967 January 17 (d = 588 km). The traces are aligned on the *ScS* arrival and the amplitudes are normalized.

As with the Okhotsk data, comparison of numerous recordings at a given station proves to be a powerful tool to eliminate misidentification of receiver phases and to increase the effective station density. The Argentine events are remarkably similar in location (Table 1) and mechanism (Table 2), so intercomparison of the events is straightfoward. Four station comparisons are shown in Fig. 33. While the *Scd* arrival is small near 72°, it is quite large near 80°, which is consistent with the Sea of Okhotsk observations. Inspection of *SH* signals at stations such as GSC and PAS for closer events confirms that the *Scd* arrival is not a receiver phase. Several of the Canadian stations are near 90°, and the waveforms at these show distinctive double arrivals in the first pulse that are generally consistent with the *Scd* and *Sab* interference seen in the Sea of Okhotsk data at similar distances. The better documented instances of this at stations FBC and EDM are shown in Fig. 34. It is interesting to note that the relative amplitude of the first and second arrivals is systematically different

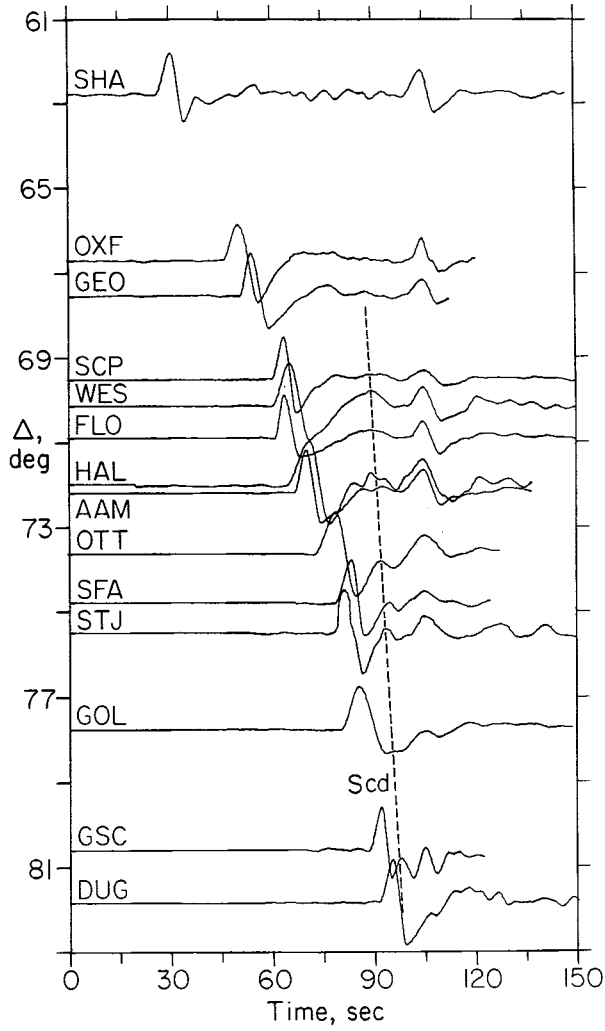

Figure 31. Profile of tangential component observations for the Argentine event of 1967 September 9 (d = 578 km). The traces are aligned on the *ScS* arrival and the amplitudes are normalized.

between the two stations. These two stations are relatively well separated in azimuth so it is possible that the change in *Scd* and *Sab* ratio is due to lateral variations in D″ within the azimuth range spanned by the North American stations.

When all *ScS–Scd* differential travel-time observations for Argentina are plotted as a function of distance, a clear *Scd* travel-time branch is defined as shown in Fig. 35. While the scatter at a given distance can be as much as 4 s, in general it is about 2 s, which is much less than the 8 s *ScS–Sab* variations. The time separation between *ScS* and *Scd* is slightly less than for model SLHO throughout the distance range 70–82°, which led us to determine model SLHA. This model has a velocity discontinuity of 2.75 per cent at a depth 27 km deeper than in model SLHO. This modification reduces the travel time difference between *ScS* and the reflection off the discontinuity and fits the Argentine data quite well in an average sense (Fig. 35). Synthetics for SLHA are compared with observations from several

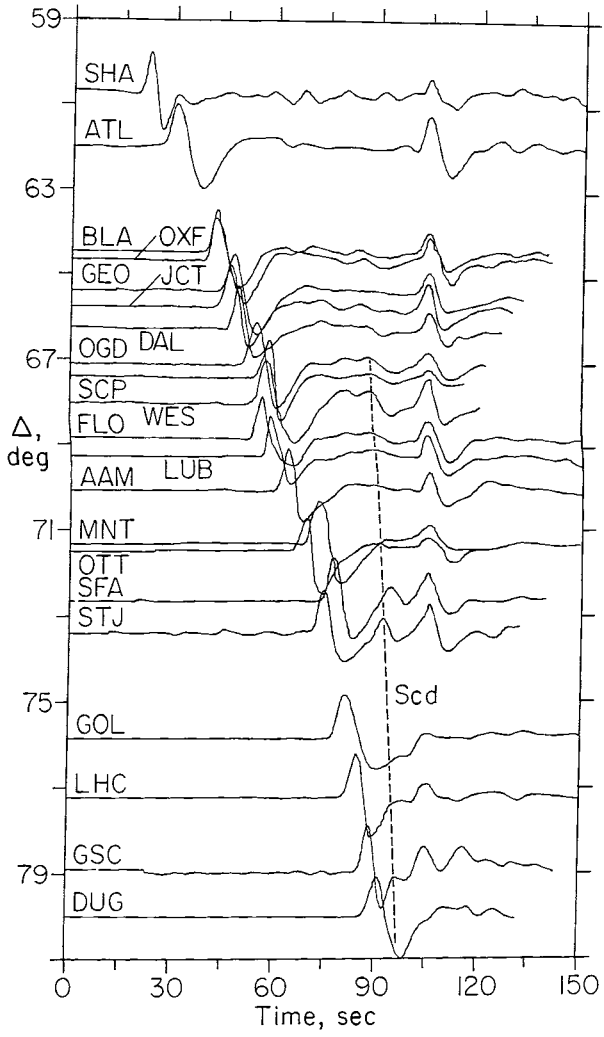

Figure 32. Profile of tangential component observations for the Argentine event of 1969 July 25 (d = 579 km). The traces are aligned on the *ScS* arrival and the amplitudes are normalized.

Argentine events in Fig. 36. The relative amplitude of the *Scd* branch throughout the range 73–80° is consistent with a velocity discontinuity the same size as in models SLHO and SLHE. The large azimuthal *ScS–S* anomalies in the Argentine data preclude the more complete waveform modelling performed for the Sea of Okhotsk observations in North America; however, SLHA provides a good average model for the Argentine paths.

Observations of the lower mantle triplication beyond crossover distance are particularly sensitive to the depth and size of the discontinuity. Thus, the observations at FBC and EDM near 90° have also been modelled. These stations require localized modifications of model SLHA. Short- and long-period observations at these stations are compared in Fig. 37. The traces have the same start time, so it is apparent that at FBC there is a small short-period precursor associated with the distortion of the long-period upswing. At EDM the first arrival is stronger on both the short- and long-period signals. These signals are

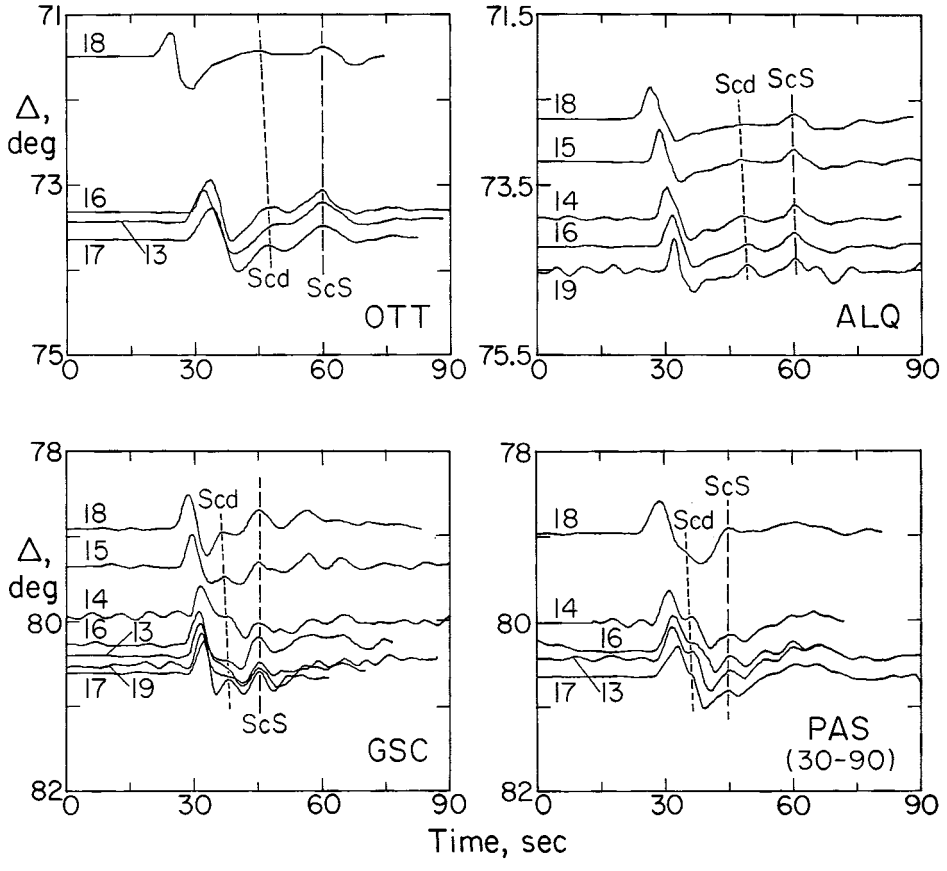

Figure 33. Comparison of observations of several Argentine events at North American stations. The numbers indicate the corresponding events in Table 1. The traces are aligned on the *ScS* arrival and the distances have been shifted as in Fig. 15. Note that the *Scd* arrival is very weak closer than 73°, but is very strong near 80°.

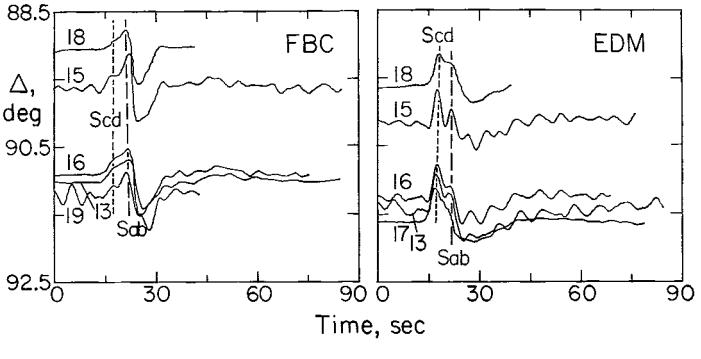

Figure 34. Comparison of *SH* observations at two Canadian stations beyond crossover distance. The numbers indicate the corresponding events in Table 1. The traces are aligned on the first arrival. Note the difference in relative amplitude of *Scd* and *Sab*.

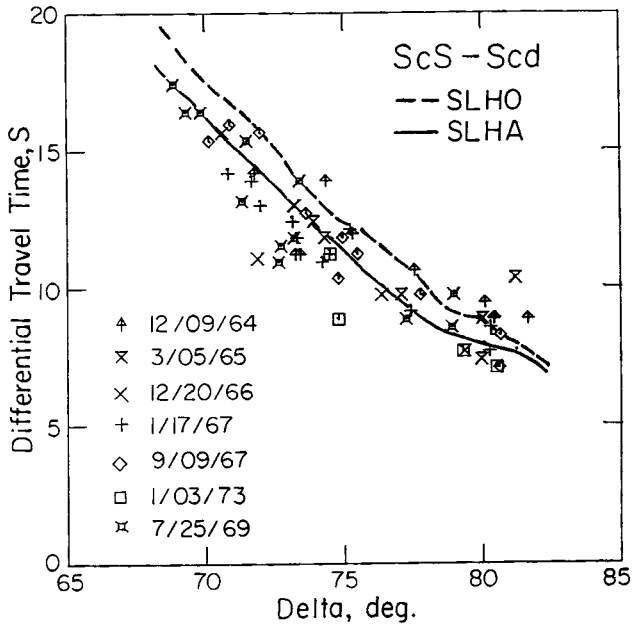

Figure 35. The peak-to-peak differential times between *ScS* and *Scd* for all the Argentine deep events. The corresponding times measured from synthetics for models SLHO and SLHA are also shown.

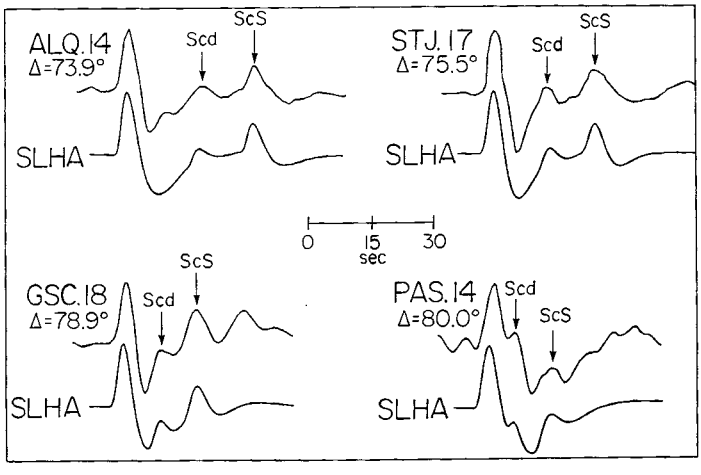

Figure 36. Observed and synthetic long-period *SH* waveforms for several Argentine events. The number after each station name indicates the corresponding event in Table 1.

generally consistent with the expected complexity near 90° for the lower mantle triplication, with the first arrival being *Scd* and the second arrival being *Sab*. However, for model SLHA, which fits the Argentine data in the range 70–82°, the *Scd* and *Sab* branches are not separated as much at 90° as seen in the FBC observations. The relative amplitudes of *Sab* to *Scd* are also not quite consistent with either FBC, for which the predicted ratio is too small, or for EDM for which the predicted ratio is too big. Since these features do not appear to be receiver structure effects, we have searched for models which can satisfy these observations near 90°.

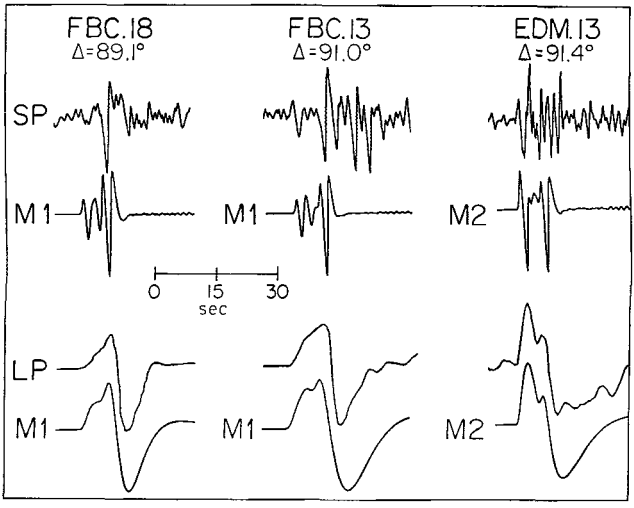

Figure 37. Comparison between the short- and long-period observations and synthetics for Argentine events in the distance range 89–91.4°. The start times of the short- and long-period traces are the same. Note the small first arrival in the FBC data compared with the strong first arrival at EDM. These features can be modelled by perturbations of model SLHA. M1 has an increased velocity contrast across the discontinuity, while M2 has a transition zone 80 km thick rather than a sharp discontinuity. Details are given in the text.

To separate the *Sab* and *Scd* branches adequately to model the FBC observations, one can either move the discontinuity to shallower depths (which shifts the crossover distance toward the source) or one can increase the velocity contrast across the discontinuity (which increases the slope between the two branches). The discontinuity must be shifted upward by nearly 100 km compared with model SLHA if the first approach is adopted, or the velocity jump can be increased to 3.8 per cent while keeping the discontinuity at a depth 280 km above the CMB. Moving the discontinuity shallower is inconsistent with the *ScS–Scd* times in the Argentine data at closer distances. The second approach yields model M1 for which synthetics are compared with FBC in Fig. 37. The time separation of the branches is in agreement with the data though the relative amplitude of *Scd* to *Sab* is still somewhat too large. Introducing a mild negative gradient throughout D″ can diminish the *Scd* branch at this distance. For EDM, the time separation between *Scd* and *Sab* is fairly consistent with the prediction for model SLHA; however, the first arrival is much stronger than predicted. To decrease the *Sab/Scd* ratio the most straightforward approach is to introduce a transition zone rather than a sharp discontinuity at the top of D″. A transition zone 80 km thick with a 3 per cent velocity increase centred 280 km above the CMB was introduced into model M2. The synthetics for this model, which is similar to SLHA, but with a distributed velocity increase, are shown in Fig. 37.

While the Argentine data do not uniquely resolve the features of models SLHA, M1 and M2, we feel that there is clear evidence for lateral variations in the lowermost 400 km of the mantle along the paths from Argentina to North America. The localized increase in velocity contrast in model M1 is very consistent with the results of Lay (1983). There it is proposed that a localized region of the lower mantle just above D″, centred below Venezuela, is about 2 per cent slower than the surrounding mantle. The paths to FBC bottom in this vicinity, thus the total velocity contrast across the discontinuity might be expected to increase. The distinctive appearance of EDM and FBC clearly requires a rather substantial lateral variation

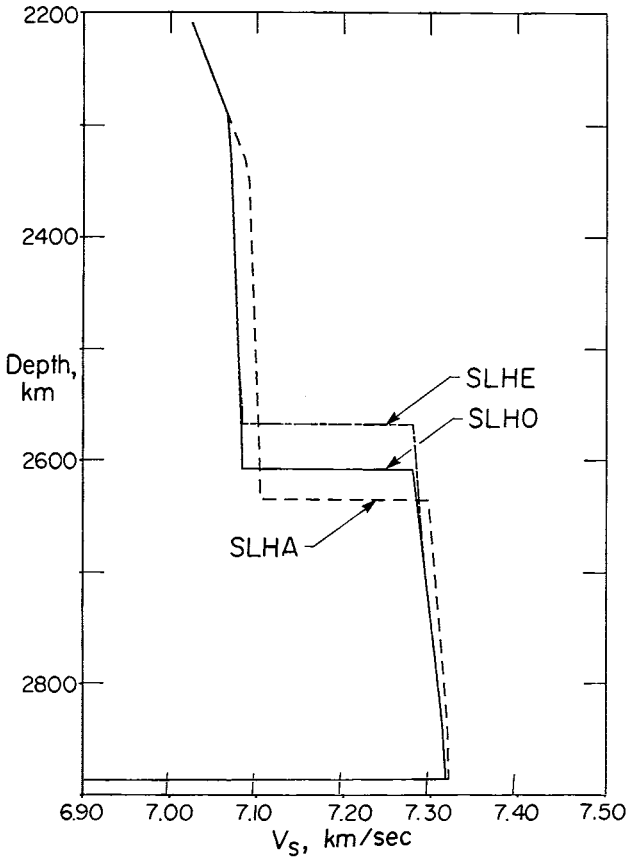

Figure 38. Comparison of the preferred shear wave velocity models that are derived for the *SH* data for each of the three source region–receiver array combinations considered. The basic feature of a 2.75 per cent velocity discontinuity about 280 km above the core is present in each case. The variations in thickness of the D″ layer are clearly indicated by the data. There appear to be lateral variations in the sharpness and size of the discontinuity in model SLHA; however, the simple model shown fits 90 per cent of the data.

in the nature of the discontinuity. Other stations in the 89–92° distance range such as COR, PNT and VIC also show the split first pulse expected at this range, but the data are too sparse to map the lateral variations in detail.

Discussion

The data from all three source region–receiver combinations analysed in this paper are consistent with the basic conclusion that a large shear velocity discontinuity exists about 280 km above the core. The models derived from the *SH* data for each sample of the D″ region are compared in Fig. 38. The basic feature of a 2.75 ± 0.25 per cent velocity discontinuity is present for each of these distinct paths. We consider these to be the first-order models, that satisfy nearly all of our *SH* observations. There appears to be lateral variation in the velocity increase and sharpness of the structure beneath northern South America represented by model SLHA; however, the basic character of the discontinuity is well established.

The similarity of the depth and size of the discontinuity in such distinct portions of the

lower mantle as investigated here does suggest that the structure is a global feature. Additional source region–receiver combinations are being investigated at present, and a final conclusion on this point must await those results. The presence of a significant, observable lower mantle feature provides an exceptional tool for modelling lower mantle lateral variations. The differences in depth of the discontinuity for the three regions discussed here are fairly well resolved, though the depths can be modified if strong lateral velocity variations within D″ are allowed. It appears more reasonable to allow some variation in the thickness of the D″ layer (which we assume to extend upward to the discontinuity). Since we are unable to constrain the density contrasts with the *SH* data alone, we cannot make conclusive arguments about whether the relief in the discontinuity is dynamically supported.

Of the published lower mantle *P* velocity models, the only one similar to the shear velocity models obtained here, is the model of Wright & Lyons (1979, 1981). Their model contains a 1.2 per cent *P*-wave velocity increase 170 km above the CMB. Below this sharp discontinuity is a strong negative velocity gradient. Most of their data are from South American events recorded at the Yellowknife (Western Canada) array. It may be possible to reconcile the difference in depth of the *P*- and *S*-wave discontinuities with lateral variations and intrinsic uncertainty in both models, and it may be possible to explain the difference in size of the discontinuities similarly or with compositional changes in Poisson ratio. However, at this point, the *P*-wave models in the literature are simply too inconsistent with one another to justify strong conclusions based on *P*- and *S*-wave model comparisons. Further work on detailed *P*-wave models is clearly required. Hopefully, this will also allow determination of the density structure of the D″ region.

The *S*-wave triplication and inferred velocity models constitute a major modification of existing lower mantle shear velocity models, but it is clear that most travel-time or diffracted *S*-wave studies would not have resolved the structure. It may be possible to detect the presence of the discontinuity in such studies if it is specifically sought. Detailed analysis of the differential times between the various branches of the triplication can be used to model lateral variations and detailed fine structure just as is done for upper mantle triplications. It is important to note that in this study, as well as in the corresponding travel-time study by Lay (1983), the major lateral variations affecting the signals appear to take place within the mantle between 600 and 2600 km depths. This is a different conclusion from previous studies which indicate that the D″ region is generally more heterogeneous than the central mantle.

The presence of a large discontinuity in the lower mantle is important for models of the Earth's thermal and compositional history, as well as for mantle dynamics. Without detailed knowledge of the density contrasts involved, it is impossible to discriminate between a phase change or a compositional change across the discontinuity. This issue is, of course, important to address, but has not been unambiguously resolved even for well-known upper mantle discontinuities. At any rate, it is quite safe to conclude that the D″ region is more complicated than a simple thermal boundary layer at the base of the mantle.

Conclusions

A large body of *S*-wave data for three source region–receiver combinations indicates the presence of a 2.75 ± 0.25 per cent shear velocity discontinuity about 280 km above the core. This discontinuity produces a triplication that can be directly observed in *SH* seismograms from intermediate and deep focus events in the range 70–95°. There appear to be lateral variations in the depth of the discontinuity of 40–50 km on a global scale; however, the triplication is quite similar for all three regions. Short-period data are consistent with either a sharp discontinuity or one distributed over up to a 50 km thick transition zone. The

presence of the discontinuity is best detected using direct *S* and *ScS* waveform information, rather than travel-time or diffracted waves.

Acknowledgments

We thank Brian Mitchell for providing his *SV/SH* amplitude inversion program, and we are especially grateful to Gerhardt Müller for providing us with a copy of the *SH* reflectivity program written by Wolfgang Schott and extensive translation of its documentation. Terry Wallace reviewed the manuscript, and provided helpful suggestions. This research was supported in part by the National Science Foundation under Grant NSF EAR 81-8616. Contribution No. 3832, Division of Geological and Planetary Sciences, California Institute of Technology, Pasadena, California 91125, USA.

References

Anderson, D. L. & Hart, R. S., 1976. An earth model based on free oscillations and body waves, *J. geophys. Res.*, **81**, 1461–1475.

Bolt, B. A., Niazi, M. & Somerville, M. R., 1970. Diffracted *ScS* and the shear velocity at the core boundary, *Geophys. J. R. astr. Soc.*, **19**, 299–305.

Bullen, K. E., 1949. Compressibility-pressure hypothesis and the Earth's interior, *Mon. Not. R. astr. Soc.*, **5**, 355–368.

Bullen, K. E., 1963. *An Introduction to the Theory of Seismology*, Cambridge University Press, London, 381 pp.

Cleary, J., 1969. The *S* velocity at the core-mantle boundary, from observations of diffracted *S*, *Bull. seism. Soc. Am.*, **59**, 1399–1405.

Cleary, J., Porra, K. & Read, L., 1967. Diffracted *S*, *Nature*, **216**, 905–906.

Doornbos, D. J. & Mondt, J. C., 1979. *P* and *S* waves diffracted around the core and the velocity structure at the base of the mantle, *Geophys. J. R. astr. Soc.*, **57**, 381–395.

Doyle, H. A. & Hales, A. L., 1967. An analysis of the travel times of *S* waves to North American stations, in the distance range 28° to 82°, *Bull. seism. Soc. Am.*, **57**, 761–771.

Dziewonski, A. M. & Anderson, D. L., 1981. Preliminary reference Earth model, *Phys. Earth planet. Int.*, **25**, 297–356.

Dziewonski, A. M. & Haddon, R. A. W., 1974. The radius of the core mantle boundary inferred from travel time and free oscillation data; a critical review, *Phys. Earth planet. Int.*, **9**, 28–35.

Fuchs, K. & Müller, G., 1971. Computation of synthetic seismograms with the reflectivity method and comparison with observations, *Geophys. J. R. astr. Soc.*, **23**, 417–433.

Gilbert, F. & Dziewonski, A. M., 1975. An application of normal mode theory to the retrieval of structural parameters and source mechanisms from seismic spectra, *Phil. Trans. R. Soc. A*, **278**, 187–269.

Hales, A. L. & Roberts, J. L., 1970. The travel times of *S* and *SKS*, *Bull. seism. Soc. Am.*, **60**, 461–489.

Helmberger, D. V., 1974. Generalized ray theory for shear dislocations, *Bull. seism. Soc. Am.*, **64**, 45–64.

Jeffreys, H. & Bullen, K. E., 1940. *Seismological Tables*, British Association for the Advancement of Science, Gray-Milne Trust, London, 55 pp.

Jordan, T. H., 1977. Lithospheric slab penetration into the lower mantle beneath the Sea of Okhotsk, *J. Geophys.*, **43**, 473–496.

Kind, R. & Müller, G., 1975. Computations of *SV* waves in realistic earth models, *J. Geophys.*, **41**, 149–175.

Lay, T., 1983. Localized velocity anomalies in the lower mantle, *Geophys. J. R. astr. Soc.*, **72**, 483–515.

Lay, T. & Helmberger, D. V., 1981. Body wave amplitude patterns and upper mantle attenuation variations across North America, *Geophys. J. R. astr. Soc.*, **66**, 691–726.

Lay, T. & Helmberger, D. V., 1983. The shear velocity gradient at the base of the mantle, *J. geophys. Res.*, in press.

Mitchell, B. J. & Helmberger, D. V., 1973. Shear velocities at the base of the mantle from observations of *S* and *ScS*, *J. geophys. Res.*, **78**, 6009–6020.

Mondt, J. C., 1977. *SH* waves: theory and observations for epicentral distances greater than 90 degrees, *Phys. Earth planet. Int.*, **15**, 46–59.

Mula, A. H. & Müller, G., 1980. Ray parameters of diffracted long period *P* and *S* waves and the velocities at the base of the mantle, *Pageoph,* **18,** 1272–1292.

Okal, E. A. & Geller, R. J., 1979. Shear-wave velocity at the base of the mantle from profiles of diffracted *SH* waves, *Bull. seism. Soc. Am.,* **69,** 1039–1053.

Press, F., 1966. Seismic velocities, in *Handbook of Physical Constants,* ed. Clark (Jr), S. P., *Mem. geol. Soc. Am. 97,* 587 pp.

Randall, M. J., 1971. A revised travel time table for *S, Geophys. J. R. astr. Soc.,* **22,** 229–234.

Robinson, R. & Kovach, R. L., 1972. Shear wave velocities in the earth's mantle, *Phys. Earth planet. Int.,* **5,** 30–44.

Ruff, L. & Helmberger, D. V., 1982. The structure of the lowermost mantle determined by short period *P* wave amplitudes, *Geophys. J. R. astr. Soc.,* **68,** 91–119.

Sengupta, M. K., 1975. The structure of the earth's mantle from body wave observations, *ScD thesis,* Massachusetts Institute of Technology, Cambridge, 578 pp.

Strelitz, R., 1975. The September 5, 1970 Sea of Okhotsk earthquake: a multiple event with evidence of triggering, *Geophys. Res. Lett.,* **2,** 124–127.

Veith, K. F., 1974. The relationship of island arc seismicity to plate tectonics, *PhD thesis,* South Methodist University.

Wright, C. & Lyons, J. A., 1979. The identification of radical velocity anomalies in the lower mantle using an interference method, *Phys. Earth planet. Int.,* **18,** 27–33.

Wright, C. & Lyons, J. A., 1981. Further evidence for radial velocity anomalies in the lower mantle, *Pageoph,* **119,** 137–162.